Feasibility-Study for Space-Based Transit Photometry using Mid-sized Nanosatellites

by

Rachel Bowens-Rubin

Submitted to the Department of Earth, Atmospheric, and Planetary Science
in partial fulfillment of the requirements for the degree of

Masters of Science in Earth, Atmospheric, and Planetary Science

at the

MASSACHUSETTS INSTITUTE OF TECHNOLOGY

June 2012

Author .....
Department of Earth, Atmospheric, and Planetary Science
May 18, 2012

Certified by .....
Sara Seager
Professor, Departments of Physics and EAPS
Thesis Supervisor

Accepted by .....
Robert D. van der Hilst
Schulumberger Professor of Geosciences and Head, Department of Earth, Atmospheric, and Planetary Science

Feasibility-Study for Space-Based Transit Photometry using Mid-sized Nanosatellites

by

Rachel Bowens-Rubin

Submitted to the Department of Earth, Atmospheric, and Planetary Science
on May 18, 2012, in partial fulfillment of the
requirements for the degree of
Masters of Science in Earth, Atmospheric, and Planetary Science

Abstract

The photometric precision needed to measure a transit of small planets cannot be achieved by taking observations from the ground, so observations must be made from space. Mid-sized nanosatellites can provide a low-cost option for building an optical system to take these observations. The potential of using nanosatellites of varying sizes to perform transit measurements was evaluated using a theoretical noise budget, simulated exoplanet-transit data, and case studies to determine the expected results of a radial velocity followup mission and transit survey mission. Optical systems on larger mid-sized nanosatellites (such as ESPA satellites) have greater potential than smaller mid-sized nanosatellites (such as CubeSats) to detect smaller planets, detect planets around dimmer stars, and discover more transits in RV followup missions.

Thesis Supervisor: Sara Seager
Title: Professor, Departments of Physics and EAPS

Acknowledgments

I would first like to thank my direct advisor, Mary Knapp, for her time, advice, and continual guidance during every part of this project. Next, I would like to thank my advisor, Sara Seager, and my thesis committee members, Richard Binzel and Josh Winn, for their discussion and feedback on my research.

Additionally, I would like to thank Jane Conner for teaching me the ins and outs of technical writing and for providing constant encouragement over the past four years.

I would also like to acknowledge my labmates Brice Demory, Julien de Wit, Rebecca Jensen-Clem, Luyao Li, Stephen Messenger, Leslie Rogers, and Matt Smith for their consultations, for supplying me with numerous resources, and for helping me prepare for my defense presentation.

Lastly, I would like to salute my friends and fellow goggleheads, Zach Barryte who taught me how to make pretty figures using Illustrator and Danbee Tauntaun Kim for her late night reassurance and support.

Contents

List of Figures

List of Tables

Chapter 1

Science Background

1.1 Purpose of Study: To determine the viability of an ESPA satellite for measuring exoplanet transits

The measurement of planetary transit events has been a powerful tool in astronomers' quest for habitable exoplanets. Although space-based missions such as Kepler are studying exoplanet transit events, the focus of the Kepler mission has been on surveying dim stars in order to gain information on the greater exoplanet population. The collection of data on planets that orbit bright stars and have a mass too small to be detected by ground observations has not received as much attention. Because these bright stars are scattered across the sky, one satellite would not be able to observe every target effectively. However, if a constellation of satellites were to be launched, many bright stars could be monitored simultaneously. Nanosatellites may provide the vehicle necessary to create such a constellation within manageable costs.

A CubeSat mission, ExoplanetSat, is being launched to perform photometric measurements on bright stars, but it will be limited in its ability to detect transits because of the size of the CubeSat platform [1]. By upgrading to a larger platform, it may be possible to increase the lens aperture size, upgrade the detector, use and collect more power, and implement other modifications requiring more mass and space. These

changes may allow a mission to probe dimmer stars to the same degree of accuracy as ExoplanetSat, allowing the mission targets list to be expanded.

The purpose of this thesis is to investigate what science missions could be accomplished if a small satellite larger than ExoplanetSat were used to do exoplanet transit photometric follow-up.

1.2 Current Methods for Detecting Exoplanets

As of May 16th 2012, 770 exoplanets have been discovered using several detection methods, including radial velocity, astrometry, transits, microlensing, direct imaging, and pulsar timing [2]. Table 1.1 gives a summary of these detection methods, the method's strength, and the number of planets that have been studied using each method.

Overall, the majority of planets have been discovered using the radial velocity method [2]. While radial velocity is a productive technique for discovering planets, the orbital inclination angle (i) cannot be determined, so the resulting values of the planetary properties are mixed with a factor of $\sin(i)$. Observing transit events of planets discovered using radial velocity can constrain the inclination angle of these planets, providing the means to improve the overall knowledge of each exoplanet.

1.3 Measuring Exoplanets via the Transit Method

1.3.1 Brightness Over Time: Implications of the shape of the light curve

When a planet passes in front of its star, a tiny but measurable amount of light from the star is blocked by the planet. The planet must be between the observer and the star in order for the planet to block the star's light and cause a transit event (Figure 1-1). If the correct alignment occurs, the observer will be able to measure the brightness of the star over time and produce a graph called a "light curve." Figure 1-2

Detection Method	Description†	Planets studied using method††	Method's Strength†
Radial Velocity	Looks for doppler shift in spectral lines from the star's movement due to planets	707*	Sensitive to large planets with short period around stars with strong spectral lines
Astrometry	Measures change in star position due to orbiting of a planet		Sensitive to large planets in wide orbits
Transit	Measures change in flux that occurs when a planet blocks light from its star	234	Sensitive to large planets with short period around bright stars
Microlensing	Measures the light distortion of a star due to the planet's gravity	15	Has very small bias for detecting planets in regards to mass and semi-major axis over 1AU
Directing Imaging	Photographs planets directly, involves screening out the light from the star	31	Sensitive to young, bright planets with large semi-major axis around dim stars
Pulsar Timing	Orbit of a planet changes the peaks in brightness coming from the pulsar and the change in time is measured	17	Can detect small planets but is sensitive to large planets with short periods

Table 1.1: *701 is the total number of radial velocity planets combined with the astrometry planets.
† Descriptions and the method's strengths are based off of the descriptions in Haswell, 2010.
†† Number of planets studied using each method were found using the Exoplanet Encyclopedia.

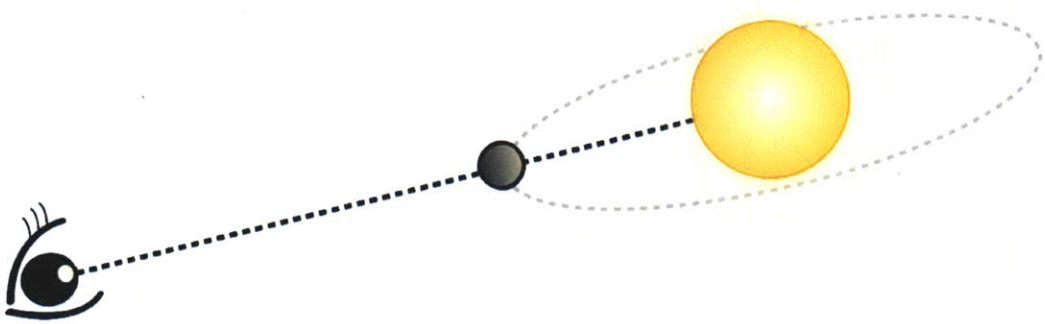

Figure 1-1: Transit Alignment. In order to measure a transit, the observer (depicted as the eye) must be aligned with the orbital plane of the transiting exoplanet and its host star. (Figure made by Zach Barryte)

depicts a light curve correlated to the movement of a planet during a transit event.

Three features of the light curve are important to determining properties of the observed planet: the transit duration, transit depth, and duration of ingress/egress (Figure 1-3 illustrates these on a light curve). From these values, the period, semi-major axis, orbital speed, orbital inclination, and radius of the planet in units of the stellar radius can be determined.

The bowl shape of the light curve is produced because of the phenomen of "limb darkening," which is discussed in greater detail in Section 1.4.2.

1.3.2 Probability of Finding an Exoplanet by Transit

As stated in Section 1.3.1, for a planet to be detected by the transit method, the orbit of the planet must be aligned such that it passes between its host star and the observer (Figure 1-1). In order for this alignment to occur, the planet must overlap the star for at least one point during its orbit. The closest approach of the center of the planet to the center of the star is when the planet is nearest to the observer (inferior conjunction). At this closest approach moment, the planet center and star center will be at a distance (d),

$$d = a\cos(i), \tag{1.1}$$

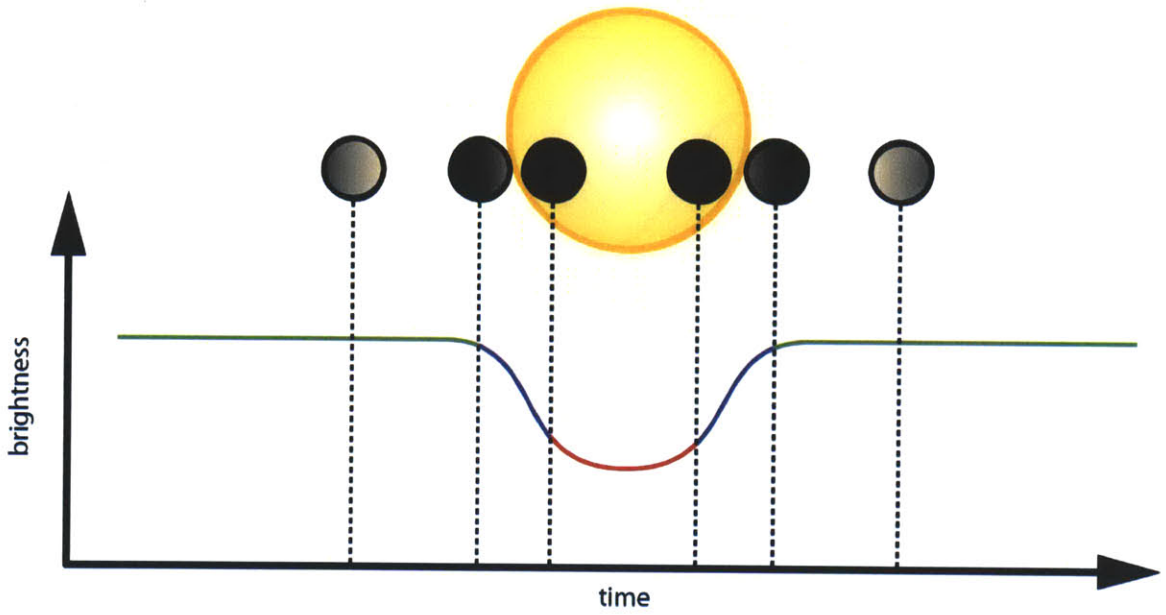

Figure 1-2: Planet Transiting a Star Correlated with the Measured Brightness. As a planet transits in front of its star, the planet blocks some of the flux emitted from the star. This change in flux can be measured (on a graph called a "light curve"). The stages of a planet in transit can be broken into three parts: "no transit" (green on resulting light curve), ingress or egress (blue), and full eclipse (red).

where a is the orbital radius of the planet which is in a circular orbit and i is its orbital inclination angle (illustrated in Figure 1-4) [3]. For the planet to block light from the star, this minimum separation distance must be within the boundaries of the combined stellar radius (R_s) and planetary radius (R_p), thus a transit occurs when

$$d = a\cos(i) \leq R_s + R_p. \tag{1.2}$$

The value of of the distance (d) can be any value between zero and the orbital radius ($0 < d < a$), but for orbits in which the planet will transit, d will be less than the combined planet and star radii ($d \leq R_s + R_p$). To find the probability of a transit occurring (P_{trans}), we can integrate over these distance values to find the ratio of the transiting orbits to all of the orbits,

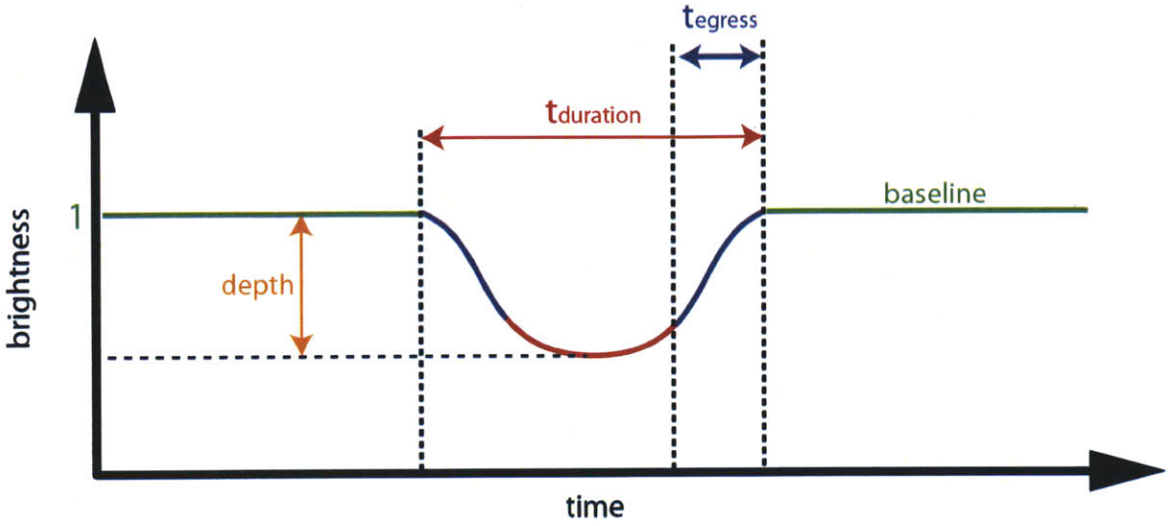

Figure 1-3: Transit Duration, Transit Depth, and Duration of Ingress/Egress. The duration of the transit is defined to be the duration of time beginning when the planet first overlaps the star and ending when the planet is completely clear of the star's radius (blue and red on light curve, red arrow). The duration of ingress (equivalent to duration of egress) is the time in which the planet moves from just overlapping the star to having its full diameter within the star (blue on light curve, blue arrow). The depth of the transit is the difference in the minimum measured flux value, which occurs at the center of the transit, and the baseline (orange arrow). The baseline flux (green on light curve) is often written normalized to one.

$$\begin{aligned} P_{trans} &= \frac{\text{Transiting Orbits}}{\text{All Orbits Possible}} \\ &= \frac{2\int_{-R_s-R_p}^{R_s+R_p} \mathrm{d}d}{\int_{-a}^{a} \mathrm{d}d} \\ &= \frac{R_s + R_p}{a.} \end{aligned} \tag{1.3}$$

Equation 1.3 reveals that the transit method has a selection bias for finding a large planet with a small semi-major axis orbiting around a large star, regardless of the quality of instrumentation. Because of this bias, an unrepresentative number of hot jupiters, hot gas giants orbiting close to their stars, have been discovered.

Using Equation 1.3 and assuming that all Sun-like stars have an Earth-like planet, we find that the probability of finding an Earth-sized planet around a Sun-sized star is

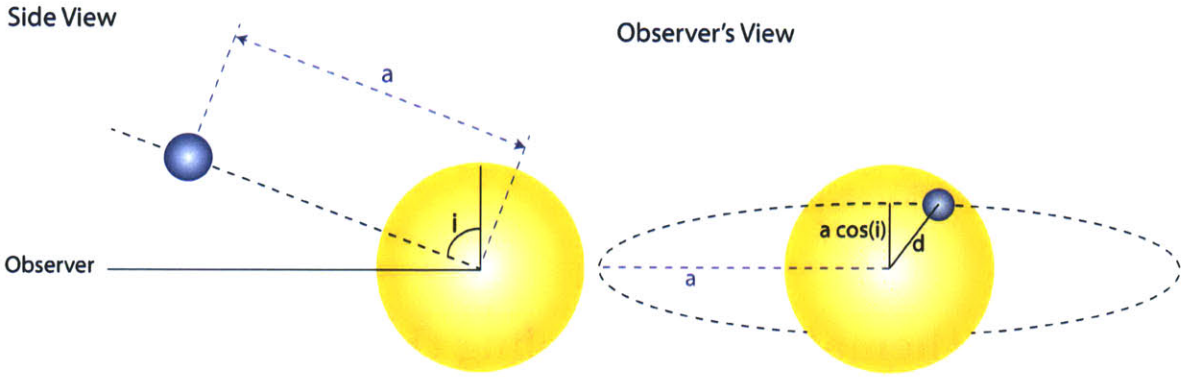

(a) Side View (b) Observer's View

Figure 1-4: Side View and Observer's View of the Planet's Orbit. The inclination angle, i, is defined to be the angle between the normal vector to the observers point of view and the planet's orbital plane. The distance, d, represents the distance the planet appears from the center of the star from the observer's point of view. At inferior conjunction, the value of d will be equal to the impact parameter, b ($d_{infconj} = b = a\cos(i)$). (Image adapted from Haswell [3])

$P_{trans} = 0.469\%$. This small percentage represents an upper-bound estimate (because not every Sun-like system will contain an Earth-like planet) and is based purely on the size, semi-major axis, and alignment of the system.

1.3.3 The Photometric Precision Threshold for Detecting a Transiting Planet

In order to declare the detection of a planet via the transit method in the Kepler survey, the photometric precision in the data must be approximately seven times smaller than the transit depth. This precision must be reached by taking data in a time duration that is less than one-half of the time of transit.

A quick estimation for the transit depth and the threshold of detection can be obtained by using the ratio of the squares of the planet radius (R_p) and the stellar radius (R_s):

$$\begin{aligned} \sigma_{Threshold} &= \frac{TransDepth}{7} \\ &= \frac{(R_p/R_s)^2}{7.} \end{aligned} \tag{1.4}$$

Using Equation 1.4 to estimate the threshold for finding Earth, we find $\sigma_{Threshold} = (8.4*10^{-5})/7 = 12\text{ppm}$. Any mission with the desire to measure a transit in an Earth-like system using the Kepler detection threshold must achieve a combined photometric precision of less than 12ppm in 6.5 hours.

1.4 Mathematically Modeling the Shape of a Light Curve

Making an exact model for the overall shape of a light curve is a geometric problem. The derivation of a model for a light curve described in this section is applied in Chapter 4 to create transit data.

1.4.1 Estimating the Overall Shape by Deriving the Eclipsed Area

The first major step to finding a mathematical model of a light curve is to get an expression for the area occulted by the planet over time. In order to find this expression for the eclipsed area, consider a planet in a circular orbit to have an orbital angular speed, $\omega = 2\pi/Period$. The planet's orbit also has a tilt, the orbital inclination angle (i), defined between the vector of the orbit and the line of sight. The distance between the star and the planet as observed "edge-on" (s) can be written in terms of i and ω by applying basic trigonometry:

$$s(t) = a\sqrt{\sin^2(\omega t) + \cos^2(i)\cos^2(\omega t)}, \tag{1.5}$$

where t represents the time since the transit midtime and a is the radius of the planet's orbit (the definitions for the variables in Equation 1.5 are illustrated in Figure 1-5).

Using the distance between the planet and star centers, we can calculate the area eclipsed geometrically by dividing the overlapping bodies into sectors. Figure 1-6 displays the geometric sectors, and labels the following variables used to calculate

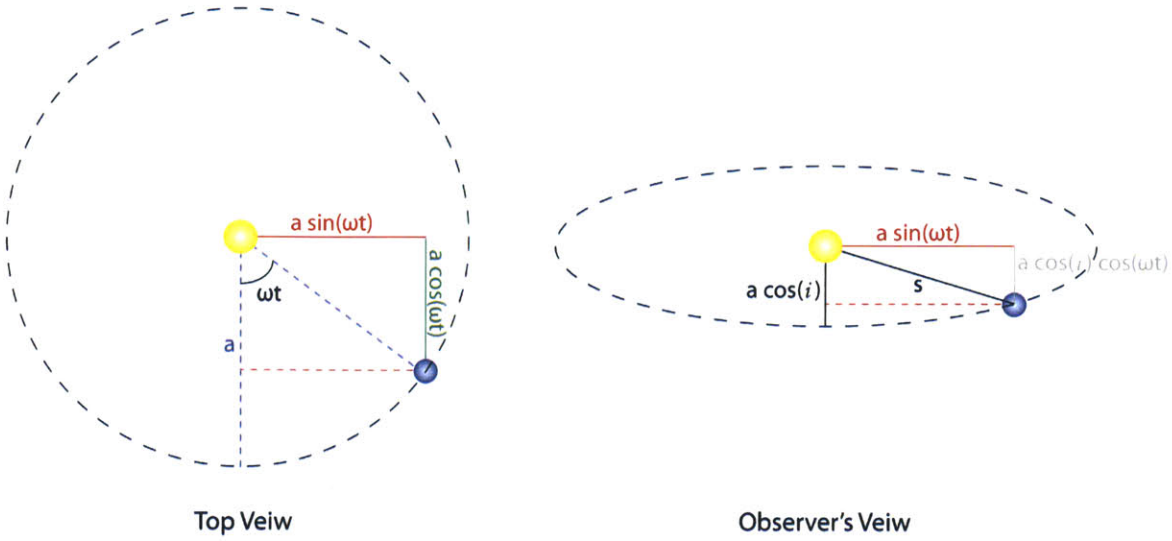

Figure 1-5: Top View and Observer's View of the Planet's Orbit. The separation of the planet and star centers, s, is the vector sum of the component in the direction of the line of sight from the observer and its perpendicular component in the planet of the sky. Although the distance of the line-of-sight component scales as a factor of $\cos(i)$ between the two perspectives (shown in green and gray), the other competent ($a \sin \omega t$) does not change (shown in red). Orbits are assumed to be a circular. (Image adapted from Haswell [3])

their areas: α_1, the angle (in radians) formed by the line segments connecting the center of the planet with the center of the star, and the planet center with the planet-star intersection; α_2, the angle formed by the line segments connecting the center of the planet with the center of the star, and the star center with planet-star intersection; Rs is the radius of the star; and Rp is the radius of the planet.

The area eclipsed can be found using three sectors (shown in Figure 1-6)):
(1)the triangle formed by the star center, planet center, and the planet-star point of intersection
(2) the circle sector of the planet between s and the planet-star point of intersection
(3) the circle sector of the star between s and the planet-star point of intersection

Adding and subtracting the areas of these three sectors will reveal one-half of the area eclipsed. Doubling this expression reveals the total area eclipsed,

$$\begin{aligned} Ae &= 2(A_{section2} + A_{section3} - A_{section1}) \\ &= 2\left(Rp^2\alpha_1 + Rs^2\alpha_2 - \frac{Rs(s)\sin(\alpha_2)}{2}\right). \end{aligned} \tag{1.6}$$

Using the Phythagorean theorem to find an expression for $\sin(\alpha_2)$, we can simplify the expression for the area eclipsed:

$$Ae = Rs^2\left(\left(\frac{Rp}{Rs}\right)^2\alpha_1 + \alpha_2 - \frac{\sqrt{4Rs/Rp - (1 + (Rs/Rp)^2 - (Rp/Rs)^2)^2}}{2}\right). \tag{1.7}$$

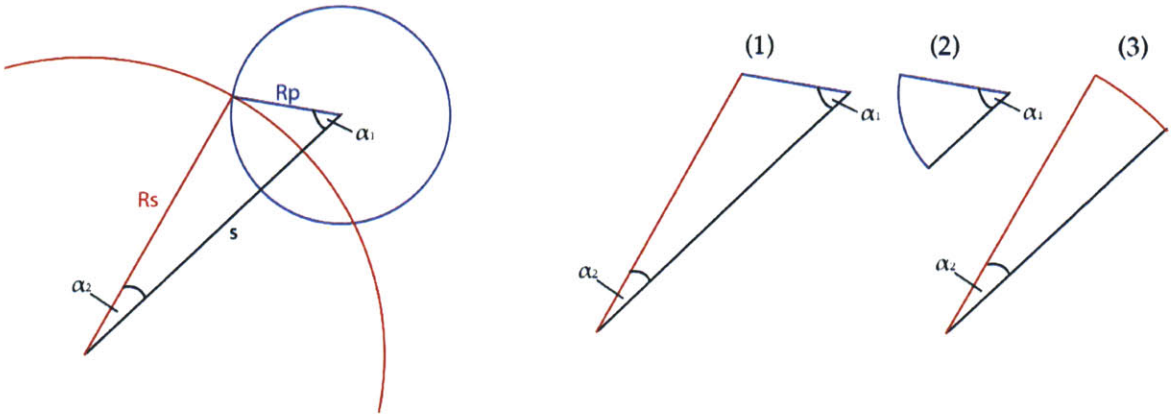

Figure 1-6: Overlapping Stellar and Planetary Disc. The definitions of the variables used to derive Equation 1.4.1 ($R_p, R_s, s, \alpha_1, \alpha_2$) are illustrated. The three regions to the right can be summed and subtracted to find the area eclipsed. (adapted from Haswell Figure 3.13, p105)

At this point, it is useful to consider the planet's orbit in three basic parts: (1) when the planet is not obstructing the star (no transit), (2) when the planet is partly in front of the star (ingress or egress), and (3) the when the planet is fully in front of the star (full eclipse). Figure 1-2 gives a representation of a planet transiting in front of its parent star and the effect it has on the measured brightness in these three stages.

(1) During the times when a transit is not occurring, no area of the star is blocked by the planet ($Ae_{no} = 0$). Because the star is not occulted, there is also no resulting

change in measured flux from the parent star (ΔF=0).

(2) In the time of full eclipse, the planet's area is fully in front of the star ($Ae_{full} = \pi R_p^2$).

(3) When the planet is in ingress or egress, the area eclipsed cannot be simplified so the entirety of Equation must be used.

Combining these three cases, the area eclipsed at any point during the planet's orbit (in the non-limb darkening case) can be described by,

$$Ae = \begin{cases} 0 & \text{if } R_s + R_p > s \\ R_s^2\left(\left(\frac{R_p}{R_s}\right)^2 \alpha_1 + \alpha_2 - \frac{\sqrt{4R_s/R_p - (1+(R_s/R_p)^2 - (R_p/R_s)^2)^2}}{2}\right) & \text{if } R_s - R_p < s \leq R_s + R_p \\ \pi R_p^2 & \text{if } R_s - R_p \leq s, \end{cases} \tag{1.8}$$

where R_s is the radius of the star, R_p is the radius of the planet, and s is the distance between the star and planet centers. The angles α_1 and α_2 can defined, using the cosine rule, as

$$\alpha_1 = \frac{R_p^2 + s^2 - R_s^2}{2R_p s} \tag{1.9}$$

$$\alpha_2 = \frac{R_s^2 + s^2 - R_p^2}{2s.} \tag{1.10}$$

1.4.2 Complications to the Overall Shape: Disconformities in the flux emitted from the solar disc

When using the approximation that a star has a uniform brightness across its surface, the area eclipsed is proportional to the change in flux ($\Delta F \propto Ae$). Thus, the depth of the transit is simply the ratio between the star's area and the planet's area,

$$\frac{\Delta F}{F} = \frac{\pi R_p^2}{\pi R_s^2} = \frac{R_p^2}{R_s^2} \tag{1.11}$$

where the fraction $\Delta F/F$ is the transit depth normalized to the baseline flux.

However, stars are not uniformly bright across their surface. For example, many stars contain sunspots, which are dimmer patches scattered in various locations on the star's surface. The limb-darkening effect, a phenomenon in which the star's edge appears dimmer and redder than the center, also adds a significant variation in brightness [3]. Both sunspots and limb darkening can be measured by transit [5], but the following model will exclude sunspots due to their wide variations across stars.

The limb-darkening effect is an outcome of the attenuation of photons traveling from the hot, blue interior of the star. Because photons traveling towards the edge of the stellar disc from the interior must travel further than photons traveling towards the center of the stellar disc, more photons from the interior escape the surface at the center of the stellar disc. The photons emitted at the edge of the stellar disc are primarily made at the cooler, redder layers nearer the limb. In order to quantify this effect, we define a term known as the "limb darkening coefficient" (μ) to be

$$\mu = \cos(\gamma), \tag{1.12}$$

where γ is the angle from the outward radial vector (shown in Figure 1-7).

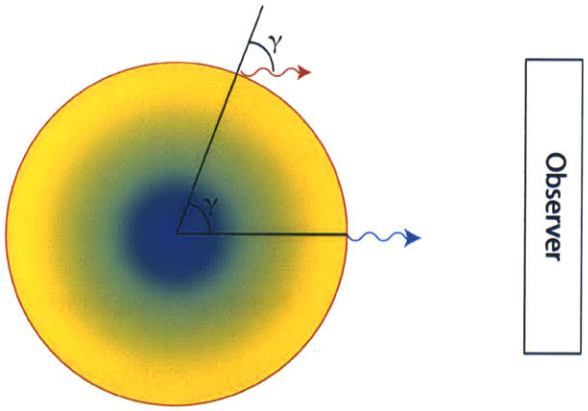

Figure 1-7: Limb Darkening Coefficient. The center of the star appears brighter and bluer than the limb. The limb darkening coefficient (μ) is written in terms of the angle from the outward radial vector (γ) (Image Adapted from Haswell, page 99)

The function between the limb darkening coefficient and the intensity radiated from the star differs for every star and can only be determined empirically or by

using stellar structure models. Different "limb darkening laws" can be applied to fit a system, the simplest of which is the linear limb darkening law,

$$\frac{I(\mu)}{I(1)} = 1 - \mu(1 - \mu) \tag{1.13}$$

where $I(\mu)/I(1)$ is the intensity normalized to the intensity at the center of the stellar disc. When applying more complicated limb darkening laws such as logarithmic, quadratic, and cubic, extra coefficients must be fit for each individual star. [3] The modeled transit data in this thesis (in Chapters 4 and 5) were created using the linear limb darkening law in order to avoid needing the values for unknown coefficients.

1.4.3 Modeling the Change in Flux, Including the Effect from Limb Darkening

By treating the stellar disc as radially symmetric, the stellar disc can be divided into annuli based on their radius, r (Figure 1-8). If each of these annuli have an infinitesimally small width, dr, the intensity will be uniform across the area of the annulus. Thus considering a series of partial annuli can turn a non-uniform flux situation into a uniform flux problem.

To find the flux change over time (ΔF) during the planet's transit, consider only the region of the annuli within the planet-star overlap. By applying Equation 1.4.1, we can calculate the area of the partial annuli by finding the area eclipsed when Rs is equal to the annulus radius, r, and a slightly larger annulus radius, $r + dr$. The difference in the values for area eclipsed at these radii is the area of the annulus (A_{dr}),

$$A_{dr}(r) = A_e(r + dr) - A_e(r) \tag{1.14}$$

where r has values between $0 \leq r \leq R_s$), as illustrated in Figure 1-8.

Once the area of each annulus is found, a weight is assigned to the annulus based on its constant intensity value at its radius value (found by applying a limb darkening law). Taking the sum of these weighted partial annuli reveals the change in flux during

the transit,

$$\Delta F = \sum I(r) A_{dr}(r). \tag{1.15}$$

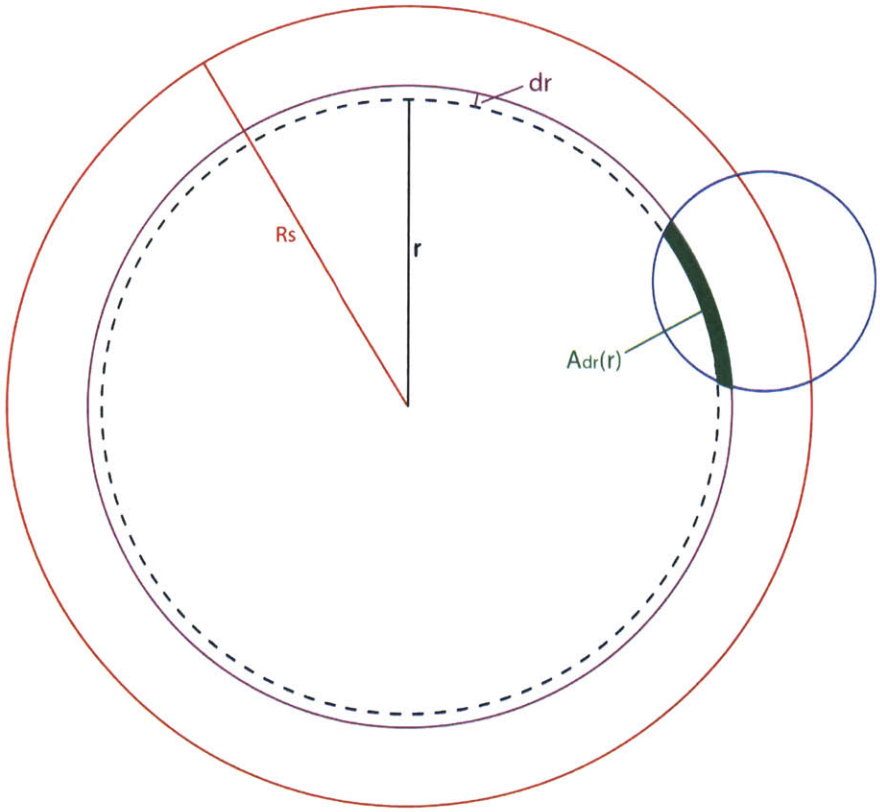

Figure 1-8: Area of Partial Annulus. The area of a partial annulus, which has a constant intensity value, can be found by subtracting the area eclipsed of a system with a stellar radius of r from another system with a stellar radius of $r + dr$.

Chapter 2

Small Satellites: a lower cost option for space missions

Because of the growing desire to build and launch satellites at a lower cost, the use of small satellites has increased in the past ten years [7]. This increase has occurred in the two smallest classes of satellites, the "pico" (mass $\leq$ 1 kg) and "nano" (1 kg $\leq$ mass $\leq$ 10 kg) class [9], and is largely due to expanding satellite programs in universities. As microelectronics, lightweight components, software, and shared launch vehicles have been improved, the cost of small satellite missions has dropped [8]. Universities and other student programs can thus fly lower-cost missions in order to perform customized experiments, test instruments and experimental technology, or fly a constellations of satellites. These types of missions can provide useful data that cannot be gathered from the ground, for example for experiments that require global coverage, zero gravity, or the absence of atmosphere.

Two types of small satellites are popular for use in the United States: EELV Secondary Payload Adapter (ESPA) Satellites and Cube Satellites (CubeSats). The ESPA system was developed by the Air Force Research Laboratory, and is now primarily used by the Department of Defense. CubeSats are smaller than ESPA-class satellites and are more popular with university and student groups, having been developed by researchers at Cal-Poly and Stanford. The MIT Aero/Astro Department has developed missions using both ESPA and CubeSats platforms (Castor and ExoSat),

which are described in sections 2.1.1 and 2.2.1.

2.1 Cubesats: a standardized pico- and nanosatellite system

In 1999, Stanford and Cal-Poly Universities introduced the specifications for the "CubeSat" program with the goal of creating a standard construction for designing picosatellites [10]. By standardizing the size and launch mechanism for these satellites, the cost of construction, the cost of launch, and the development time can be reduced while still allowing for custom payloads.

The standard size for a CubeSat is a 10x10x10-cm cube (1U) with each cube weighing up to 1.33 kg in mass. Larger CubeSats can be constructed in a lego-like fashion by stacking cubes into 2U (22x10x10cm) and 3U (34x10x10cm) sizes. Figure 2-1 shows the exteriors of the 1U, 2U, and 3U kits which buyers can purchase if they want a standard CubeSat exterior.

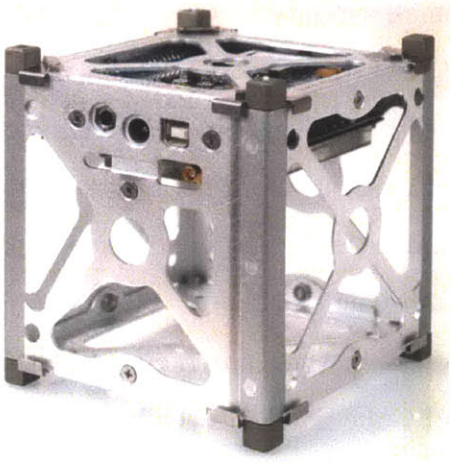

(a) Pumpkin 1U CubeSat Exterior

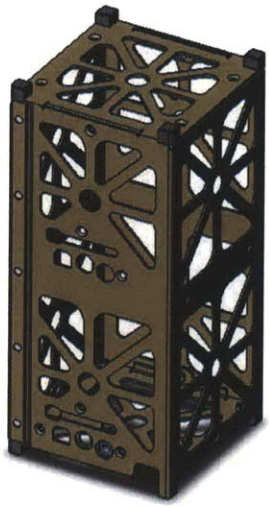

(b) Pumpkin 2U CubeSat Exterior Model.

(c) Pumpkin 3U CubeSat Exterior

Figure 2-1: 1U, 2U, and 3U CubeSat Designs. The company Pumpkin sells CubeSat kits which buyers can use to decrease manufacturing time and costs. The exteriors of some of the kits are shown here. The 1U kit is approximately the size of a small kleenex box. [11]

The most popular deployer for CubeSats, the Poly Picosatellite Orbital Deployer (P-POD), can launch up to 3-units of cubesat satellites (Figure 2-2). The P-POD attaches to a primary launch vehicle, and the CubeSats are carried to space as a secondary payload. Special precautions are taken so that the CubeSat deploy does not damage the primary launch vehicle including P-POD-CubeSat interface testing, requiring CubeSats be loaded into the deployer uncharged, and thermal and vibration testing [10]. A new 6U version of the P-POD is being developed to accommodate more and larger CubeSats [7].

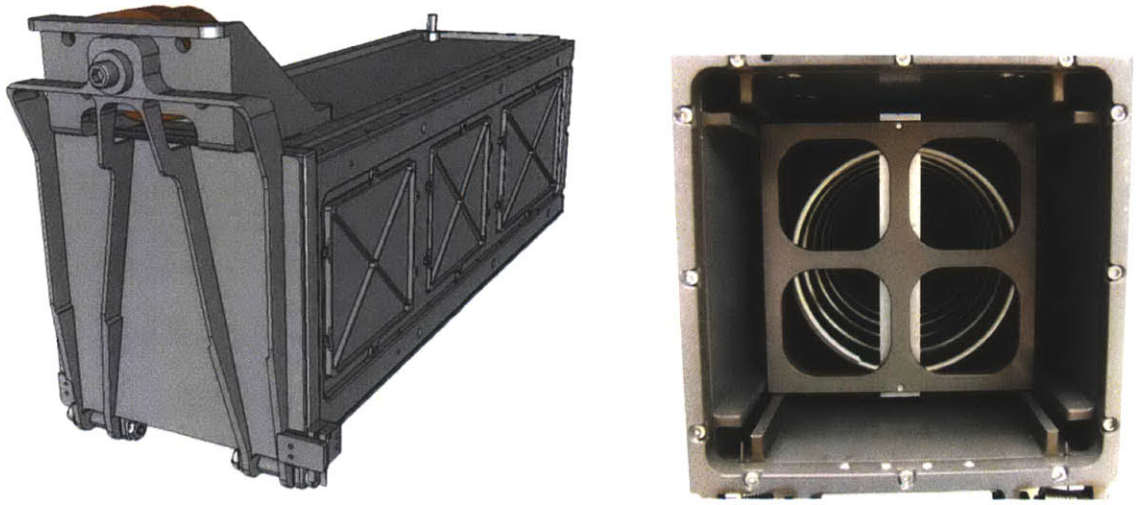

Figure 2-2: Poly-Picosatellite Orbital Deployer (P-POD) Schematic and Inside. The P-POD deployer can hold 3U of cubesat satellites and is designed to hold any CubeSat which follows the CubeSat specifications. Once in space, springs force the door open and the main spring pushes the satellites out of the deployer, sliding along the guide rails. [10]

Since the emergence of CubeSats, several missions have performed quality research using this platform. GeneSat and PharmaSat were developed by NASA Ames to study the effects of radiation and low gravity on bacteria and yeast, respectively [12] [13]. QuakeSat, developed by Stanford, searched for extremely low frequency magnetic signals that are a precursor to earthquakes, in order to try to detect earthquakes

[14]. Atmospheric research has been performed by a number of missions, such as SwissCube-1 and UNICubeSAT, and the number of missions continues to grow [7].

2.1.1 ExoplanetSat: a 3U CubeSat capable of observing exoplanet transits

Continuing the trend of doing significant science with CubeSats, ExoplanetSat (or ExoSat) is a 3U CubeSat designed to take photometric data of transiting exoplanets. The goal of ExoSat will be to monitor bright Sun-like stars in order to perform follow-up measurements of planets discovered by the radial velocity method. Once a prototype is proven, a constellation will be launched in order to monitor the bright stars scattered across the sky [1].

The design of ExoSat began as part of an undergraduate course in the Aeronautical/Astronautical Engineering and Earth, Atmosphere, and Planetary Science Departments at MIT. Since the end of the class, the development of ExoSat has been continued by researchers at MIT as well as Draper and Lincoln Laboratories.

Although ExoSat plans to take data of exoplanet transits, it is limited by the size of the CubeSat platform. The lens aperture in the 3U CubeSat will be 7.7-cm, limiting the satellite's observational abilities to collect photons. Larger satellites taking photometric data separate the star-tracking imager from the science imager, however ExoSat is combing these two systems into one detector to save space. To achieve the fast imaging rate needed for star tracking, ExoSat will use a complementary metaloxidesemiconductor (CMOS) chip to collect science data; however, this chip is less sensitive than other chips usually used in astronomy, so the collection of photons is less efficient. With a larger platform, it may be possible to both increase the aperture size and use a more efficient science detector.

(a) ExoSat with its solar panels deployed. [1]

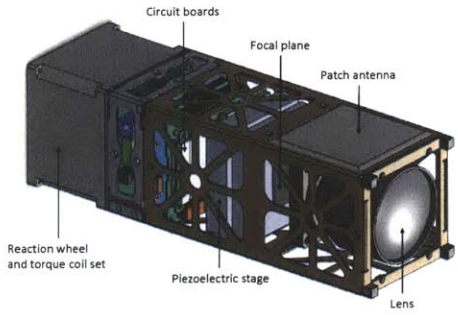

(b) Inner components of ExoSat. [15]

Figure 2-3: Diagrams of the ExoSat Design.

2.2 ESPA Satellites: a larger standardized satellite system alternative

The Evolved Expendable Launch Vehicle (EELV) is a launch system developed by US Air Force used to launch satellites for the Department of Defense. In late 1990s, the Air Force Research Laboratory designed the EELV Secondary Payload Adapter (ESPA) so secondary payloads could be launched with a primary payload (Figure 2-4 shows the EELV-ESPA interface) [16].

The most common type of ESPA ring can hold six secondary payloads of up to 181 kg and approximately 61-cm x 61-cm x 96-cm in volume (Figure 2-5). However, ESPA rings can also be constructed in a variety of dimensions and with varying numbers of docking rings [16]. The EPSA ring can merely provide a vehicle for the launching of secondary payloads, or satellites can be integrated with the ring, providing a structure for instruments. If more space is desired, ESPA rings can be stacked [17].

NASA made use of the ESPA technology in 2009 when it launched the Lunar CRater Observation and Sensing Satellite (LCROSS) [18]. LCROSS flew as a secondary payload to the Lunar Reconnaissance Orbiter with the goal of studying hydrogen at the polar regions of the Moon. The spacecraft used the ESPA ring for structure to support six instruments/ power and control system parts and was built of primarily of off-the-shelf components. It was able to take visible, infrared, and

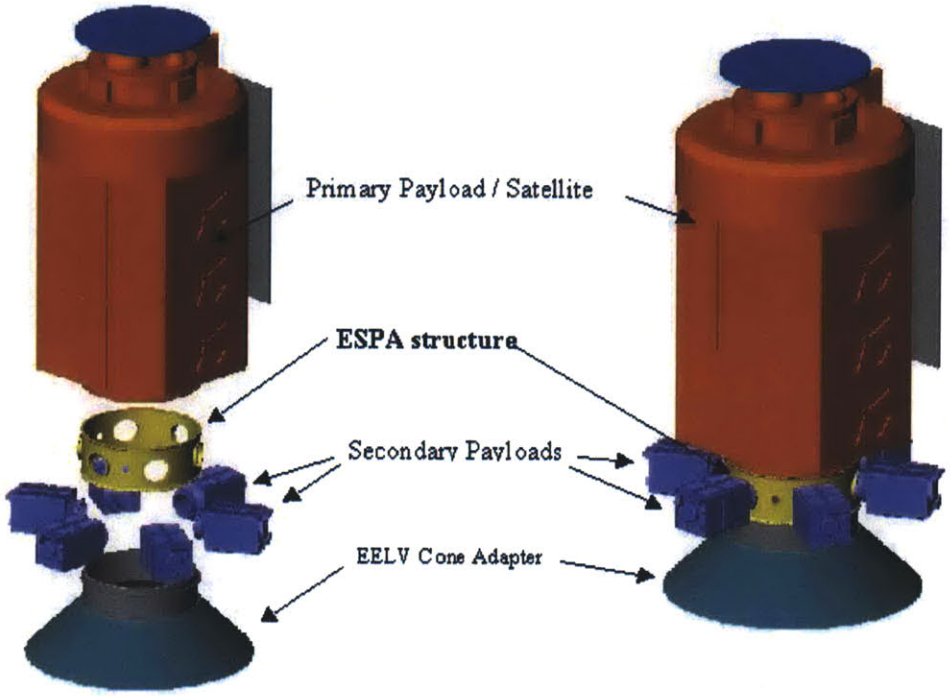

Figure 2-4: EELV-ESPA system. The ESPA is placed directly between the primary payload and the EELV. The EELV-ESPA is approximately the height of a one-story building. (Image from the ESPA Design Specifications [16])

Figure 2-5: Model of an ESPA ring with Six Docking Rings. This ESPA ring allows six secondary payloads to be launched with the primary spacecraft. The ring is approximately the diameter of a bus tire.(Image from the ESPA Design Specifications [16])

near-infrared images of the Moon (including the first infrared image of the far side of the moon) before impacting the surface to create a plume of Moon material. The

LCROSS mission received a number of awards, and demonstrated that ESPA rings can be used successfully to produce low-cost science missions.

2.2.1 Castor: an ESPA spacecraft with the potential to be repurposed

The Cathode/Anode Satellite Thruster for Orbital Repositioning (Castor) satellite was a mission to test a new thruster system (Figure 2-6 shows a basic model of Castor). This satellite was developed by the MIT Aero/Astro department as part of the same undergraduate course as ExoSat, with the support of the University Nanosat Program (UNP) contest. However, Castor was not selected for launch in the UNP contest, likely due to the risk of the Castor payload design and the mission goal of Castor.

Thus, parts from the 50-cm x 50-cm x 60-cm ESPA-class satellite still remain at MIT, which could be repurposed to fit a different need and save money and time. Redesigning this spacecraft to do space-based photometry is under consideration.

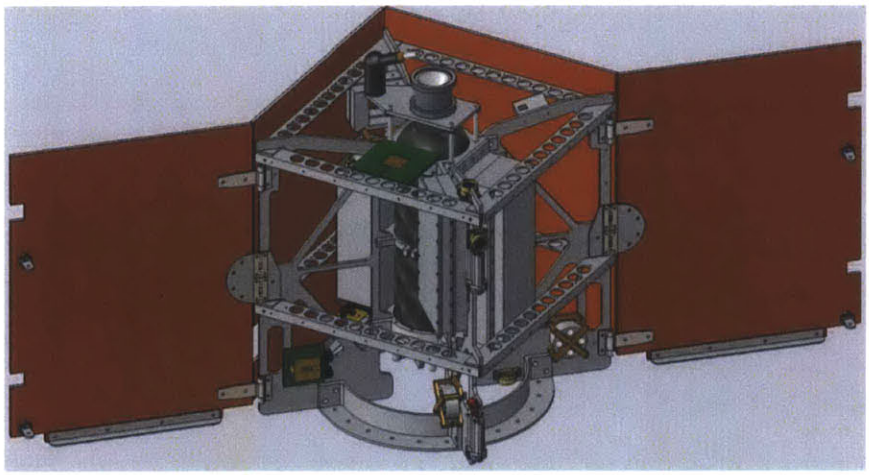

Figure 2-6: Model of Castor, an ESPA satellite designed at MIT. Castor, originally designed to test a new propulsion system, was never launched. Redesigning this spacecraft for taking photometric astronomical data is under consideration. (Image from the Castor Satellite Design Document [19])

Chapter 3

Creating a Noise Budget for Space-Based Transit Observations

3.1 Important Choices for Engineering Systems

In order to achieve the best photometric precision possible, decisions about the engineering systems must be made carefully. Section 3.1 outlines some of the basic choices that must be made, how the environment of the satellite may be affected, and how I chose to model these choices and environments.

3.1.1 Detector: CCD versus CMOS

Two types of imaging detectors were considered for the construction of the noise model: complementary metal oxide semiconductors (CMOS) and charged coupled device (CCD). CCD detectors have outperformed other types of imagers which can be used for collecting astronomical data for decades. However, the CMOS technology is becoming comparable in its power to collect and transfer charges with low additional noise.

CMOS and CCD chips both harness the photoelectric effect to collect photons over an area and convert them into a signal, keeping spatial and intensity information. The main difference between CMOS and CCD detectors is the way each imager

processes signals. While the two detectors both collect photoelectrons in pixels, CCD detectors transfer the photoelectrons in rows and then convert the charge to a voltage signal after the transfer; CMOS chips convert the charge to a voltage signal at each pixel. This parallel processing allows CMOS chips to read very quickly, but it also adds more read noise into the system. Typically, CMOS imagers beat CCDs in settings where fast readouts are necessary or in environments with high radiation levels. However, CCD detectors usually have an advantage in collecting photons because they have higher quantum efficiency (photon-to-photoelectron conversion), a larger well capacity, and a better ratio of light-collection-area to electronics.

The Cypress HAS2 detector was chosen to represent CMOS imagers in my noise model, and the CCID41 detector from Lincoln Labs was chosen to represent CCD detectors. These detectors were chosen for study because they are high quality, well characterized, and available to researchers at MIT for use in satellites. The properties of the detectors that are important to the error budget are listed in Table 3.1.

Characteristic	CCID41 Value	HAS2 Value	Units
Pixel size	24	18	[um]
Pixel well capacity	250000	100000	[e-/pixel]
Quantum efficiency	0.7	0.45	[0 - 1]
Fraction the pixel well should be filled	0.6	0.8	[0 - 1]
Rows	1024	1024	[#]
Columns	1024	1024	[#]
Temperature	0	25	[C]
Dark current	1130	244	[e-/s/pixel]
Plate scale	58.2	43.7	[arcsec/pixel]
Read noise	5.0	50.0	[e-/pixel]
Maximum read rate	2.5	10.0	[Hz]
Minimum integration time	0.4	0.1	[s]
Gain temperature sensitivity	unknown	800	[ppm/ΔC]

Table 3.1: Detector Characteristics and Electronics of the CCID41-CCD detector and the Cypress HAS2 CMOS detector. [20] [21]

3.1.2 Optical System

The optical system refers to the elements used to focus light on the detector. Telescopes use two main varieties of optics, reflective and refractive. Reflective optical systems use curved mirrors to focus light onto the detector, while refractive optics use lenses [7].

It is unclear whether a reflective or refractive system will be better suited for use in an mid-sized nanosatellite, so for ease of modeling I used parameters from the Zeiss Planar T 85 f/1.4 lens, which will be used in ExoSat.

3.1.3 Orbit Type: Low Earth Orbit

For simulations of data collection, the satellite was modeled to be in a low Earth orbit (altitude $<$ 2000km). A low Earth orbit (LEO) was chosen because most CubeSats are launched in this region [9].

As the satellite orbits, it will pass through a time of orbit day and orbit night. "Orbit day" refers to the period of time when the sun is shining directly upon the satellite. This time can be used to collect solar energy to power the communications system, guidance system, and the payload in the satellite. "Orbit night" is when the satellite is in the Earth's shadow and can be used to perform observations. For a low Earth orbit, the orbit day will last approximately 60 minutes, and the orbit night will last approximately 30 minutes.

It is unlikely that a satellite will be able to observe for the entirety of an orbital night because of temperature stabilization and power usage, so I assumed that observations would last for a duration of 20 minutes during orbital night in various points in the analysis.

3.1.4 Temperature Fluctuations: Using a Thermal Control System

The temperature of satellites in low Earth orbit fluctuate because of the orbit day-night cycle. During the day, when the satellite is exposed to the sun, the spacecraft

rises in temperature; but during the orbital night, the spacecraft radiates heat and cools.

ExoSat is expected to fluctuate $\pm 2°C$ during one orbital cycle, if the temperature is left uncontrolled [22]. To mitigate this fluctuation, ExoSat will use a temperature control system. To model the temperature variation in the satellite, I used the best values of the temperature fluctuation that the temperature control system in ExoSat could achieve (4.5 millikelvin, with a systematic error of 2.9 millikelvin) [22].

3.2 Contributing Sources of Error

To make an estimate for the total noise in the system, seven potential sources of noise was evaluated: shot, background light (zodiacal), dark, read, gain, quantization, and jitter (Figure 3-1). Shot noise and background light noise are forms of natural noise, which are caused by the uncertainty in the production of photons. Dark, read, gain, and quantization noise depend on the design of the detector system. Jitter noise is connected to the variation in pixel sensitivity of the detector coupled with the satellite's ability to hold itself in a constant position.

The total contribution of these noise sources were evaluated given varying inputs of aperture size, target star magnitude, detector type, and desired light curve time resolution.

3.2.1 Shot Noise

Shot noise (or "photon noise") is a result of the inherently random process of photon creation. When an electron moves from a higher to lower energy level, a photon is created. For an individual electron, the timing of this process cannot be predicted; however, for an ensemble of electrons, the average number of photons created in a period of time will remain constant. The histogram photon creation represents a Poisson distribution. The maximum of the Poisson distribution (what we measure as the total signal) is related to the standard deviation of the the distribution (what we measure as the shot noise),

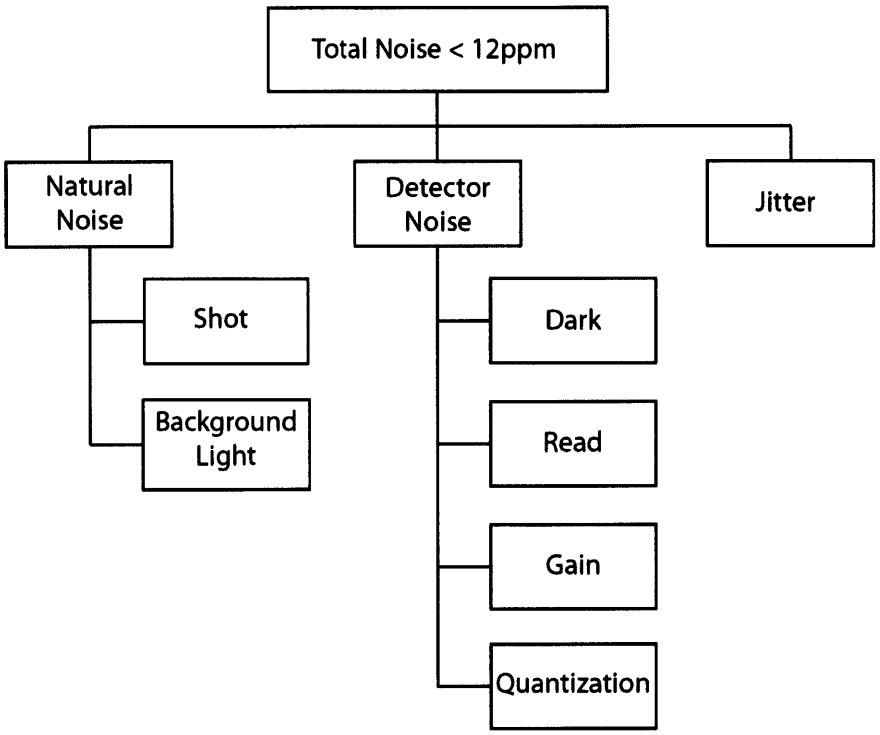

Figure 3-1: Total Noise Budget. Sources of noise for the natural collection of photons, detector properties, and jitter noise will combine to create the total noise budget. (Image adapted from Jensen-Clem, ExoSat Design Doc)

$$\begin{aligned} \sigma^2_{shot} &= S_{tot} \\ &= PhotArrRate_{targ} \times t \end{aligned}$$

where S_{tot} is the total signal, t is the time spent receiving photons, and the $PhotArrRate_{targ}$ is the number of photons arriving per second from the target star. An increase in the signal-to-noise ratio (SNR),

$$\begin{aligned} SNR &= \frac{S_{shot}}{sigma_{shot}} \\ &= \sqrt{PhotArrRate_{targ} \times t}, \end{aligned} \tag{3.1}$$

requires either an increase in the amount of time spent collecting photons, or a change

to the system's design to increase the photon arrival rate.

The photon arrival rate of the target star ($PhotArrRate_{targ}$) is dependent on the magnitude of the target star (m_{targ}) and the area of the lens aperture (A_{apt}),

$$\begin{aligned} PhotArrRate_{targ} &= PhotArrRate_{ref} \times 10^{-(m_{targ}-m_{ref})/2.5} \\ &= (F_{ref} \times A_{apt}) \times 10^{-(m_{targ}-m_{ref})/2.5} \end{aligned} \tag{3.2}$$

where F_{ref} is the flux and m_{ref} is the magnitude of a reference star (for the calculations in this thesis, Vega was chosen as the reference star). The reference flux is dependent on values related to the engineering choices of the optical system including the quantum efficiency of the detector (QE), the passband (or wavelength range that is being studied), and the lens throughput (or how much signal is allowed to pass through the lens).

Therefore, increasing the photon arrival rate requires either brighter target star, a large lens aperture, or a detector with a higher quantum efficiency. To increase the shot noise SNR without increasing the photon arrival rate, data must be collected for a longer period of time.

I will not consider cases in which the passband or lens throughput are changed, and I will only consider the two values for the QE as listed for the CCID41 and HAS2 in Table 3.1 (the QE for the CCID41 is approximately double the QE of the HAS2 detector). I will consider aperture sizes between 5-cm (ExoSat sized) and 45-cm (maximum reasonable size for an ESPA-class satellite).

3.2.2 Dark Current

Thermal energy causes electrons to spontaneously become free from the insulating areas of the detector and be read with the photoelectrons stored in each pixel. The number of electrons randomly generated is known as the dark current and can be calibrated out of the reading. However, because the electron generation process is random, there is an additional Poisson noise that is introduced to the system. [23]

Similar to shot noise, the dark error (σ_{dark}) depends on the number of particles produced, which in this case is the dark current (N_d),

$$\sigma_{dark} = \sqrt{N_d}. \tag{3.3}$$

The rate at which the dark current accumulates increases as temperature increases based upon a Fermi distribution ($\frac{\partial N_d}{\partial t} \propto T^{3/2}\exp(T^{-1})$). Therefore, the generated dark current and error from the dark current will be smaller at lower temperatures. [23]

For my model, I chose a detector temperature of 0°C (as described in Section 3.1.3) and scaled the dark current values listed on the specification sheets accordingly. The values for the dark current in the CMOS chip were higher than the CCD because exposure times for the CMOS were longer (visible in the total error budget in Figure 3-5). Overall, the dark current noise did not significantly contribute to the total noise.

3.2.3 Read Noise

As the signal from each pixel is processed by the amplifier and the analog-to-digital-converter (ADC) in the detector, random additions of electrons introduce "read noise" into the system. The read noise of the system is strongly correlated with the speed at which the signal is being read. During fast reads, a higher amount of noise is introduced; thus, it is advantageous in reducing read noise for the detector to read slowly. However, reading the detector slowly loses signal collection time. A balance must be found between having a low-noise readout and using time effectively to collect photons. [23]

Read noise is introduced for every reading of a pixel, so it is most efficient to wait until a pixel is at its maximum capacity before reading it. Detectors with a deep pixel well capacity and a high desired well capacity will need to be read less frequently. Although the desired well capacity of the Cypress HAS2 is higher than the CCID-41, the well capacity of the CCID-41 is large enough to compensate for and exceed the

HAS2 when it comes to the maximum electron capacity per pixel. The CCID-41 can collect photons for longer periods of time without taking a reading.

Due to the construction and fast readout rate of CMOS chips, the Cypress HAS2 detector has a read noise an order of magnitude larger than the CCID-41 detector (see Table 3.1).

3.2.4 Jitter Noise

As the detector is taking an image, the satellite has slight variations in its pointing. These small movements change the position at which photons hit the detector (Figure 3-2). If the detector was perfectly uniform, this would not be a problem; however, the quantum efficiency varies across pixels (inter-pixel variation) and within the pixels themselves (intra-pixel variation). Because of this non-uniformity, noise is introduced into the system.

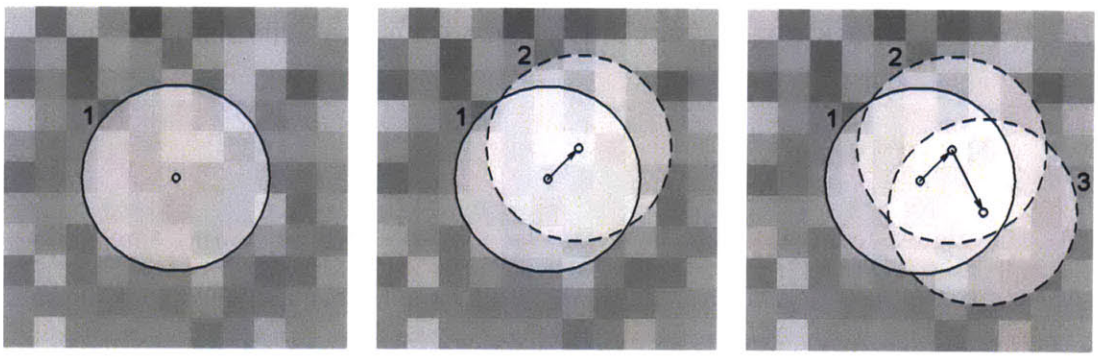

Figure 3-2: Spot Motion on the Detector. Over a very short period time, the image will move to around the detector, changing places between and within pixels. Because of the detector non-uniformity (represented by the squares of different shades of gray), the signal from a constant source will appear to vary. (Image source Smith, 2010 [1])

Although jitter noise is a combination of inter- and intra-pixel variation, the variation within the pixel is usually more problematic. If the pointing control is within the pixel size, the photons will hit the same pixel and the inter-pixel variation will not matter. The inter-pixel variation can also be calibrated by taking flat field images.

The jitter noise is also dependent on the number of pixels the image is spread over, which is controlled by the defocus setting. Using a small defocus setting spreads the

image over many pixels and decreases the jitter noise.

Jitter noise is independent of the integration time above a threshold known as the "pixel correlation time." Below the pixel correlation time, the image may appear to wander in random paths due to pointing changes. Above the pixel correlation time, a consistent blob of path appears (Figure 3-3). The independence of integration time extends to independence of star magnitude and aperture size.

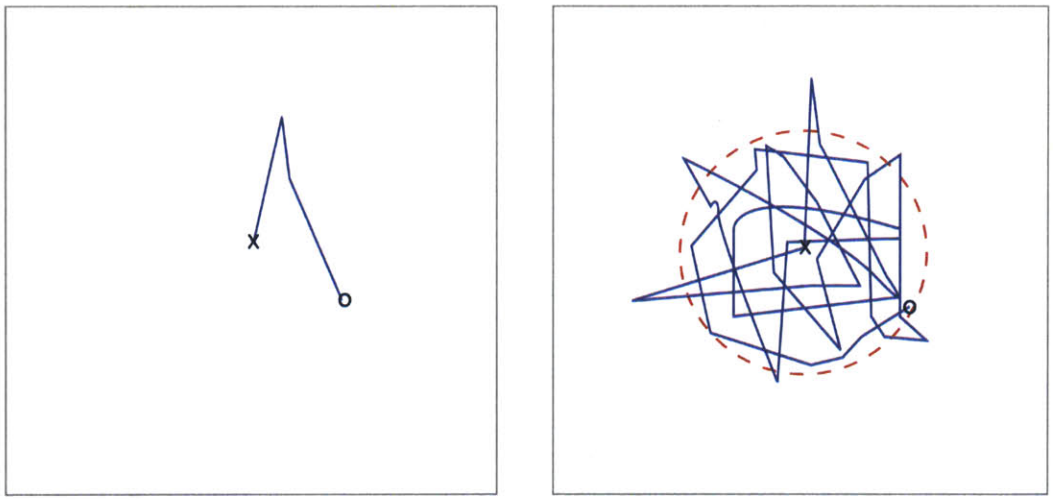

Figure 3-3: Pixel Correlation Time. Because the satellite pointing is not perfect, the center of the image will move around the detector (represented by the blue path). (Left) Below the pixel correlation time, the center of the image appears to wander randomly. (Right) Given a period of time longer than the pixel correlation time, the center of the image is more quantifiable. The diameter of red circle is the jitter amplitude, the amount by which the satellite pointing varies.

The jitter noise estimates used in my noise model were based on empirical simulations made by Matt Smith for ExoSat [1]. These estimates represent an upper bound estimate for a more massive satellite, because the pointing is easier to control in systems with more mass. For ExoSat the pixel correlation time is approximately 0.2 seconds. Because the integration times are seldom shorter than this (and not physically possible with the CCID41), I estimated the jitter noise as constant.

3.2.5 Quantization Noise

In the readout process, the collected signal is converted from an analog to a digital signal. When this conversion occurs, the analog input voltage is rounded to a digital output value of a limited specificity. This rounding process introduces "quantization noise." Figure 3-4 shows an example of what happens to similar inputs in the analog-to-digital conversion (ADC).

In a uniform analog-to-digital conversion, the window size for the input signal rounding will remain constant (for example, the input will always be rounded to the nearest hundredth). For non-uniform ADCs, the window size may vary over different input levels (for example, some inputs will round to the nearest hundredth while others round to the nearest tenth). [26]

The quantization noise was on the order of one-hundredth of the total noise, and thus was insignificant.

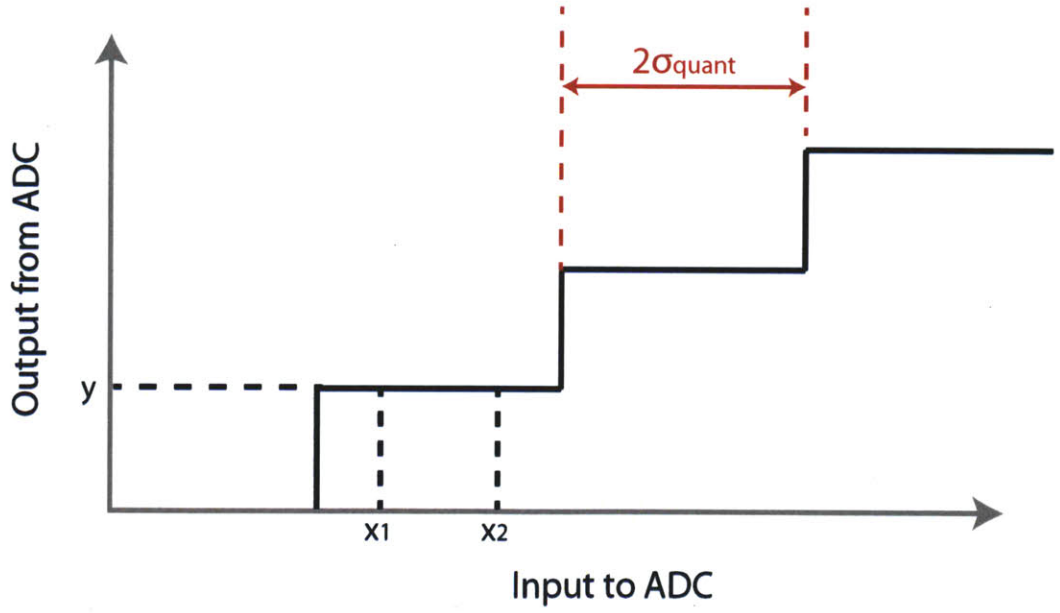

Figure 3-4: Quantization Noise: Input and Output signals into the ADC. Although x_1 and x_2 represent different input signals, the output signal is the same value, y. The uncertainty caused by this imperfect conversion (σ_{quant}) is taken to be one-half of the total step size. The better the ADC, the smaller the step sizes will be (a perfect conversation would appear linear).

3.2.6 Background Light

Although satellites in space are above most of the atmosphere, the light from the Sun still causes a glow in the background of images. Light scattered off of interplanetary dust produces a glow in space of approximately 21 Vmag/arcsec^2 in low Earth orbit with variations with position on the sky. Like shot noise, the zodiacal noise is random and Poisson by nature ($\sigma_{zod} = \sqrt{S_{zod}}$), because it is dependent on the random creation of photons.

In my model, I estimated the stray light from the Earth and Moon to also be equal to the zodiacal noise. This estimate may be optimistic, but the final estimate will depend on the size chosen for the baffle.

3.2.7 Gain Drift

The gain is the measurement of the amplification which the signal gets when it is converted from analog to digital (electrons to voltage). It is formally defined by the ratio of the number of electrons going into the ADC to raise the voltage output by one ADU (analog-to-digital unit).

Unfortunately, the gain is highly dependent on the temperature of the detector. Unless the temperature is precisely controlled, the gain drift can add significant systematic and nonsystematic errors into the data set. For example, the estimated noise caused by the gain drift of the Cypress HAS-2 detector is 800 ppm/ΔC [20]. For a small satellite like ExoSat, the temperature fluctuation without a temperature control system was modeled to be as high as $\pm 2\Delta$C [22]. In this case, the gain drift could add a massive 3200ppm to the noise budget if the data analysis did not calibrate for any systematic error. Thus having a precise temperature control system is essential for collecting the extremely precise data need to detect Earth-sized planets.

The best temperature control achieved by the system developed for use in ExoSat held the detector temperature constant to within 4.5 millikelvin, with a systematic error of 2.9 millikelvin. For ExoSat, this would be an unreasonable value to expect in flight (because these values were obtained using very controlled lab conditions),

but for a larger satellite this level is more achievable. Assuming that an ESPA-class satellite can achieve this highest quality of precision and all of the systematic trends can be calibrated, the gain noise would not be a large contribution to the total noise (Figure 3-5). However, if this level of temperature control cannot be reached, the noise from the gain drift quickly would become a dominating noise source.

Information about the gain drift for the CCID41 could not be found, so the CCD gain drift was modeled using the estimates for the Cypress HAS2.

3.2.8 Noise Sources Not Modeled

This model did not take into account the following potential noise sources:

Temperature dependent: output amplifier offset drift, quantum efficiency drift, opto-mechanical drifts. These were not modeled because it was assumed that the temperature control in the satellite is good enough to keep these noise sources at an insignificant level.

Read Irregularities: ADC integral nonlinearity, Integration timing error, Ghost images, Trapped / deferred charge, Vignetting gradient. These irregularities were not considered because hardware is available to reduce the problematic effects if they occur.

Natural Noise Dependent on Target Star and Field: Modeled noise sources in comparison stars (e.g. shot, dark, read, etc.), intrinsic variability of the target star, intrinsic variability of comparison stars, Charged particle hits. It was assumed that target stars could be selected carefully to have a good field of comparison stars and very low variability.

3.3 Calculating the Total Noise

3.3.1 Total Error Budget

The evaluated noise sources (including shot, dark, read, jitter, zodiacal, quantization, and gain drift noise) were added in quadrature to get an estimate for the total noise,

$$\sigma_{tot} = \sqrt{\sigma_{shot}^2 + \sigma_{dark}^2 + \sigma_{read}^2 + \sigma_{jitter}^2 + \sigma_{zodiacal}^2 + \sigma_{quant}^2 + \sigma_{gain}^2}. \tag{3.4}$$

The dominant noise sources were jitter (for bright stars) and shot noise (for dim stars). If the temperature is not controlled precisely, the noise from the gain drift could become a dominant noise source; however, for the temperature fluctuation modeled (± 1.6 millikelvin), the gain drift does not dominate.

The contributing noise sources plotted with total error are shown in Figure 3-5 for the HAS2 and the CCID41 detectors. Overall, the CCID41 detector was able to achieve a better photometric precision than the HAS2 at all aperture values.

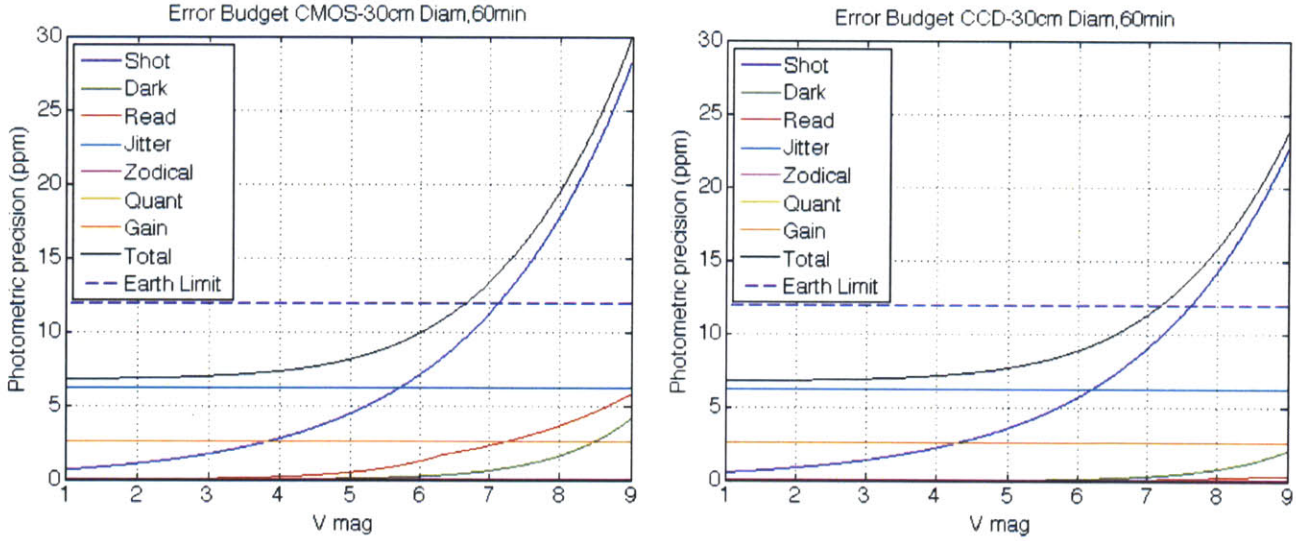

(a) CMOS Error Budget. The Earth-like planet detection limit is reached at 6.7 mag.

(b) CCD Error Budget. The Earth-like planet detection limit is reached at 7.2 mag.

Figure 3-5: Sources of Error for Time Resolution of One Hour and Aperture Size of 30-cm. The two largest contributing sources to the total error are the jitter noise (for bright stars) and the shot noise (for dimmer stars). When using the same aperture size, the total noise level for the CCD is lower, so Earth-like planets can be detected around dimmer stars with the CCD. A time resolution of one hour was chosen because it is equivalent to three orbit nights of data. An aperture size of 30-cm was chosen because 30-cm is a conservative estimate for what aperture size could be used in an ESPA-class satellite.

3.3.2 Effect of Aperture Size, Target Magnitude, and Time Resolution on Total Noise

Increasing the aperture size, the time resolution, and the brightness of the target star lowered the total noise.

Figure 3-6 demonstrates the effect on the total noise related to varying the aperture size and the target star magnitude. Interestingly, there is an asymptote in the total noise level which cannot be passed by increasing the aperture size or target star brightness. This asymptote is caused by the constant value of the jitter noise, and it is only affected by changing the time resolution or the design of the satellite to lower the jitter value.

In order to detect an Earth size planet, the choices for aperture size, observational cadence, and the brightness of the target star must combine to lower the photometric precision to a level of 12ppm. Figure 3-7 demonstrates the levels needed for the aperture size and the target star magnitude given time resolutions of 5, 20, 30, 60, and 180 minutes. By choosing a time resolution, we can extract the dimmest star for which we can still detect an Earth-sized planet at select aperture sizes (Tables 5.4 and 5.5).

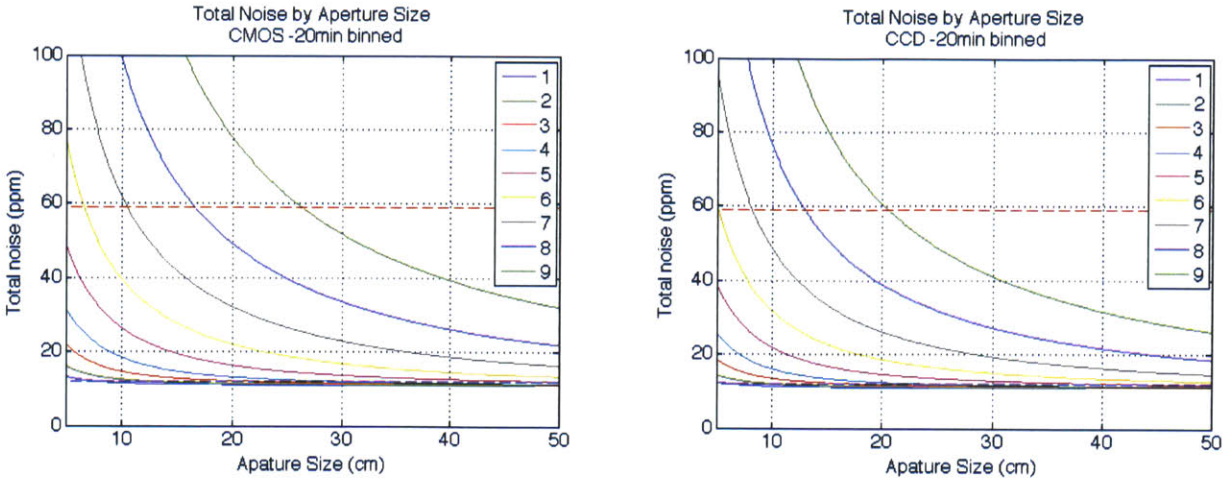

(a) CMOS (b) CCD

Figure 3-6: Total Noise Estimate varying by Aperture Size for a collection duration of 20 minutes. The red dotted line represents the photometric precision needed to observe 55 Cancri E (59ppm), and the blue dotted line represents the photometric precision needed to detect an Earth-sized planet (12ppm). All aperture sizes greater than 20-cm can detect a 55 Cnc e-sized planet down to ninth magnitude. Because jitter noise is independent of target star magnitude, the lines of varying target star magnitude (solid lines of different colors) reach an asymptote slightly under 12ppm for both the CMOS and CCD.

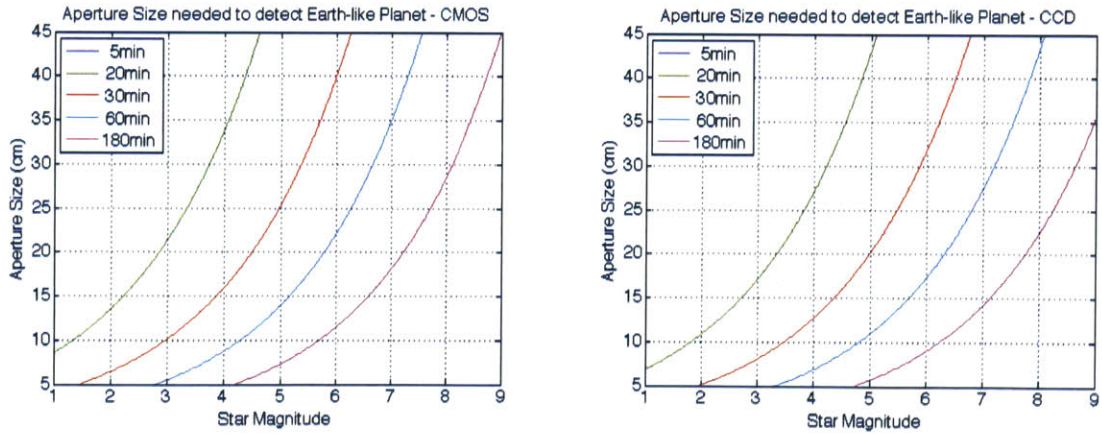

(a) CMOS (b) CCD

Figure 3-7: Aperture Needed to make a 7σ detection of an Earth-Sized Planet. For larger aperture sizes and longer observational cadence times, Earth-sized planets can be detected around dimmer stars. The photometric precision using an observational cadence of 5 minutes is not small enough to make a detection of a planet as small as Earth at any aperture size, so the 5 minute line does not appear on the graph.

Chapter 4

Simulating Data of Exoplanet Transits Collected from Space-Based Missions

A transit simulation code, based off the derivation in Section 1.4, was written in order to give a visual representation of how a satellite's orbit and physical characteristics would affect the quality of the data. The simulations account for the overall transit structure, orbit day and night, and the noise models created in Chapter 3. Collecting multiple transits, stacking, and binning were also simulated.

This chapter uses the planet 55 Cancri E as an example case. This planet has a period of less than a day and is approximately Earth sized, making it ideal to demonstrate a photometry on a short time scale.

4.1 The Overall Shape of the Light Curve

The baseline, ingress/ egress, and the total eclipse of transits can be graphed, following the derivation described in Chapter 1, for non-limb darkening and linear limb darkening. The non-limb darkening structure and linear limb darkening structure for transits of 55 Cancri E are shown in Figure 4-1.

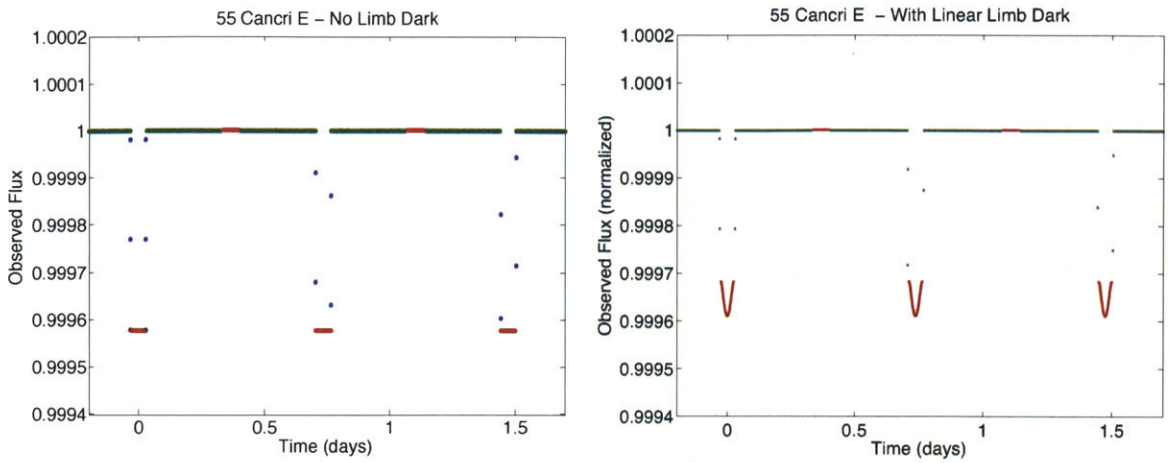

(a) No Limb Darkening

(b) Linear Limb Darkening

Figure 4-1: Shape of 55 Cancri E Transit. The green indicates the time of no transit, the blue indicates when the planet is partly in front of star, and the red indicates when the planet is completely in front of star or completely behind the star. Points are spread 1 minute apart. Secondary transits are not accounted for but would appear in the region where the red points equal the baseline.

4.2 Adding Noise Consistent with the Error Budget

The total noise estimates (found in Chapter 3) were applied to make a visualization to compare the transit depth to the expected photometric precision. The total noise was estimated using a combination of the expected values for shot, background light (Zodiacal), dark, read, gain, quantization, and jitter noise.

Figure 4-2 shows a 55 Cancri E transit using the photometric precision using a 30-cm aperture diameter and the CCD detector for a one-minute data cadence. These conditions represent what could be achieved using an ESPA-class satellite.

The total noise source was estimated to be Gaussian (white) and thus does not account for any systematic errors.

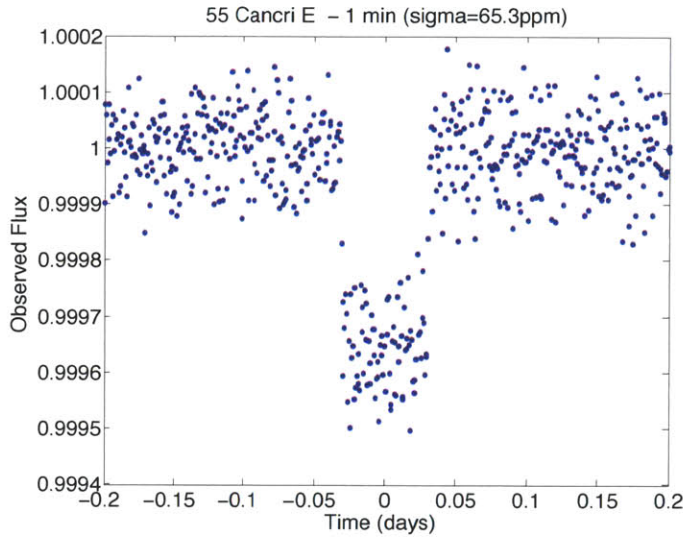

Figure 4-2: 55 Cancri E with error, one-minute data cadence.

4.3 Gaps Due to Orbit Day and Night

As the satellite orbits, it will pass through a time of orbit day and orbit night. "Orbital day" is when the sun is shining directly upon the satellite and "orbital night" is when the satellite is in the Earth's shadow. The satellite will only observe during part of orbital night, so there will be gaps in the observed light curves.

Figure 4-3 shows the sections of a 55 Cancri E transits which will occur during orbital day and orbital night. Figure 4-4 shows only the region of the transits which will be occurring during orbital night and would thus be observable. A low Earth orbit (60-minute day, 30-minute night) was assumed.

4.4 Stacking Transits and Binning to Improve the Photometric Precision

In order to fill in the gaps in the observed light curve due to orbital day, multiple transits can be collected and stacked on top of each other. Four transits must be collected in order to have a visible window to observe the entirety of a 55 Cancri E transit. More transits would need to be observed to fill the gaps when the entire

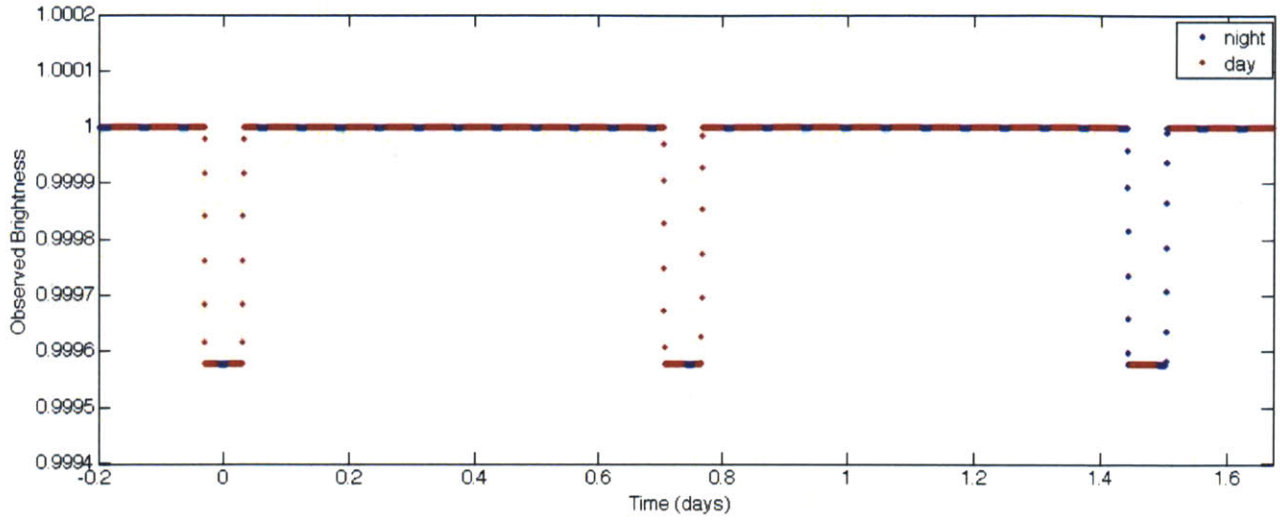

Figure 4-3: 55 Cancri E Transit with Orbit Day and Night. Orbit day is shown in red (60 minutes) and orbit night (30 minutes) is shown in blue for example 55 Cancri E transits. Points are spread 20 seconds apart, and no limb darkening was applied.

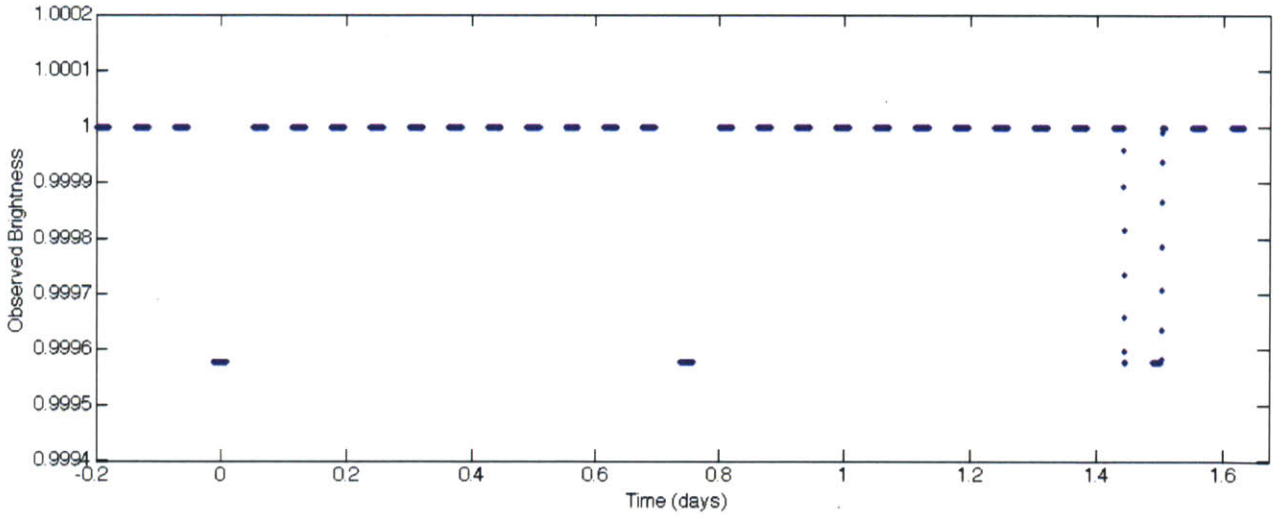

Figure 4-4: 55 Cancri E Transit with only Orbit Night Data. The satellite can only gather transit data during part of the orbit night periods, so gaps will be seen in the observed light curve. The blue points represent the entire duration of orbital night, the maximum time one could gather data. Points are spread 20 seconds apart, and no limb darkening was applied.

orbital night period is not being used for data collection. Figure 4-5 displays the progression as four 55 Cancri E transits are stacked on top of each other.

In order to raise the overall signal-to-noise ratio, the data from multiple transits

can be binned. When points are binned, the error on the combined point (σ_{binned}) becomes

$$\sigma_{binned} = \frac{\sigma}{\sqrt{n},} \tag{4.1}$$

where σ is the original error and n is the number of points that were combined. A set of binned data is shown in Figure 4-6.

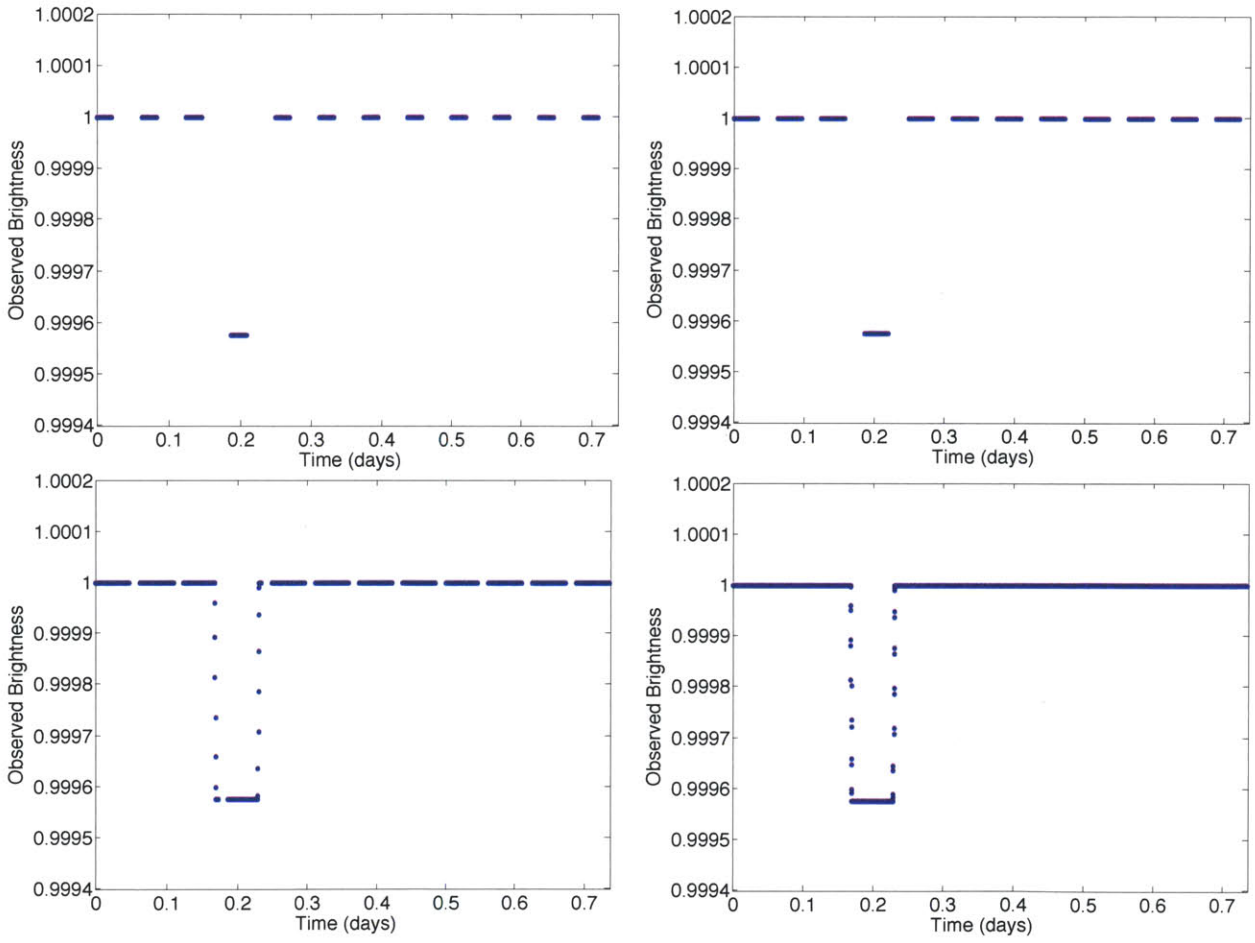

Figure 4-5: Stacking Transits. One, two, three, and four transits are stacked on top of each other, eliminating the gaps due to the satellite's orbit. The stacked transits shown are based off of the basic outline of 55 Canacri E, with no error and no limb darkening. The ingress/egress phase is not visible in one-half of the transits.

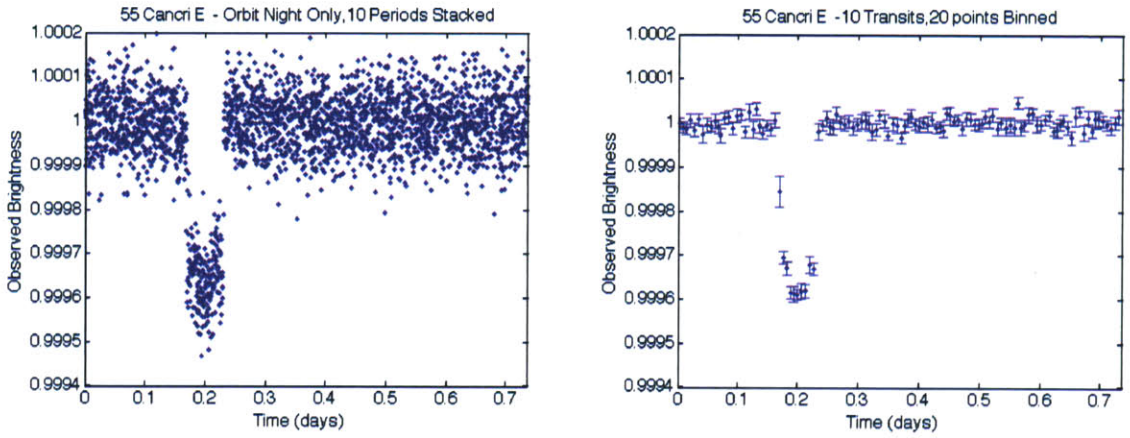

(a) 10 Transits Stacked

(b) Same 10 Transits Binned

Figure 4-6: Ten 55 Cancri E transits Stacked and Binned. Assuming a collection time of 20 minutes every orbit, ten 55 Canacri E transits with a data cadence of 1 minute were stacked and binned. Twenty points were binned together, creating a data cadence of 20 minutes

Chapter 5

Radial Velocity Follow-up and Transit Survey Case Studies

A case study was performed to demonstrate what can be achieved by a potential mission using an ESPA satellite (aperture size of 30-cm) to measure transits of known RV planets. The goal of this case study was to

(1) determine the frequency for which transits of planets may be observable,

(2) simulate the data which could be obtained by such a mission, and

(3) gain an estimate for how many planets could be discovered transiting.

To accomplish Objective (1), calculations were made to predict observable-transit times between January 1st, 2014 and January 1st, 2015 for potential target planets. The outcome of the observable-transit simulations were used to simulate transit data (Objective (2)).To explore Objective (3), the error budget created in Chapter 3 was applied to determine a list of target candidates. The probability for each candidate to transit was calculated and applied to create the probability distribution for the mission as a whole to detect a transit.

In addition to exploring the potential outcome of an RV-followup survey, the expected results of a general transit survey to discover planets which transit G and K type stars was examined. The number of potential stars that could be monitored and the expected planet haul was calculated for satellites with aperture sizes between 5-cm and 40-cm.

5.1 Determining the Frequency of Observable Transits

A theoretical observation plan was created to gain an estimate for the frequency of observable transits. The results from this section depend only on the science targets and not the specifications for the spacecraft; thus, these results can be applied to an RV follow-up mission using any size or type of satellite.

5.1.1 Selecting Targets and Finding Transit Windows

In order to form an observation plan, a list of planets discovered using the RV method was assembled. The planets orbiting bright (<7 magnitude) Sun-like stars were selected to be potential candidates.

For each bright star candidate, estimates for the transit midtime and duration were calculated using the properties found via RV studies including the period, eccentricity, time of periastron, and the argument of the periastron. The estimates for the given target list were made by Mary Knapp and Brice Demory using data from the Exoplanet Encyclopedia [2]. Planets without the necessary measured values needed to calculate the midtime were removed from the candidate list. The final list of candidates, containing nineteen planets, is listed in Table 5.2.

Once the transit midtime and duration of one transit was found, a series of "transit windows" were constructed using the measured period of the planet. These transit windows predict the times the planet may have a visible transit. The transit windows for HD20794b, HD20794c, and HD20794d during 2014 are shown in Figure 5-1. The example windows account for one-sigma measurement errors on the midtime and duration, but do not propagate the error on the period over the course of a year (if this error was propagated, the transit windows would be wider at the end of the year). Extra time to collect baseline data was also not included, because the timing of the collection of baseline data is flexible, and the one sigma error margin will allow some baseline data to be taken within the transit window.

5.1.2 Orbit Model and Observable Windows

The orbit of the satellite will affect the "observable windows" of the target stars. Thus, in order to discover these observable windows, a simulation for the orbit must be performed. Satellite Tool Kit software (STK) was used to find the observable window for each of the potential target stars. The parameters chosen for the orbit simulation are shown in Table 5.1. These parameters where chosen to optimize the creation of a generic low Earth orbit with no extremes. The result for the observable window of the star HD20794 is shown in Figure 5-1.

The observability of stars is affected by the position of the Earth, Moon, and Sun. These bodies will block stars with low declination values during portions of the year.

As stated in Chapters 3 and 4, the satellite will only observe during a portion of orbital night. This will cause gaps in the transit data (Figure 4-4). This effect is noticeable in the observable windows for each star (Figure 5-2 shows a zoomed-in observable window for HD20794 where this effect is visible).

Orbital Element	Value	Units	Meaning
Eccentricity	0	-	Orbits with an eccentricity value of 0 are circular
Altitude	500	km	Height of orbit from the surface of the planet, 500km is in LEO
Inclination Angle	45	deg	Measure of angle of orbit plane from a plane through the equator. Possible values range from 0 to 90°
Cone Angle	14.5	deg	Measure of the field of view width
Graze Angle	22	deg	How close you can get to the moon/sun/earth and still observe a star
Observable Window per Orbit Night	20	min	Amount of time data collection occurs every orbital period

Table 5.1: Parameters for Simulated Orbit

5.1.3 Observable-Transit Windows: When Transits can be Observed

The intersection between the visibility of the star and the time the planet is predicted to transit creates an "observable-transit window." This observable-transit window can be found by overlaying the observable window and the transit window and finding their points of intersection. The observable transit window for the planets around HD20794 is shown in Figure 5-1, along with the overlapping windows used to make it.

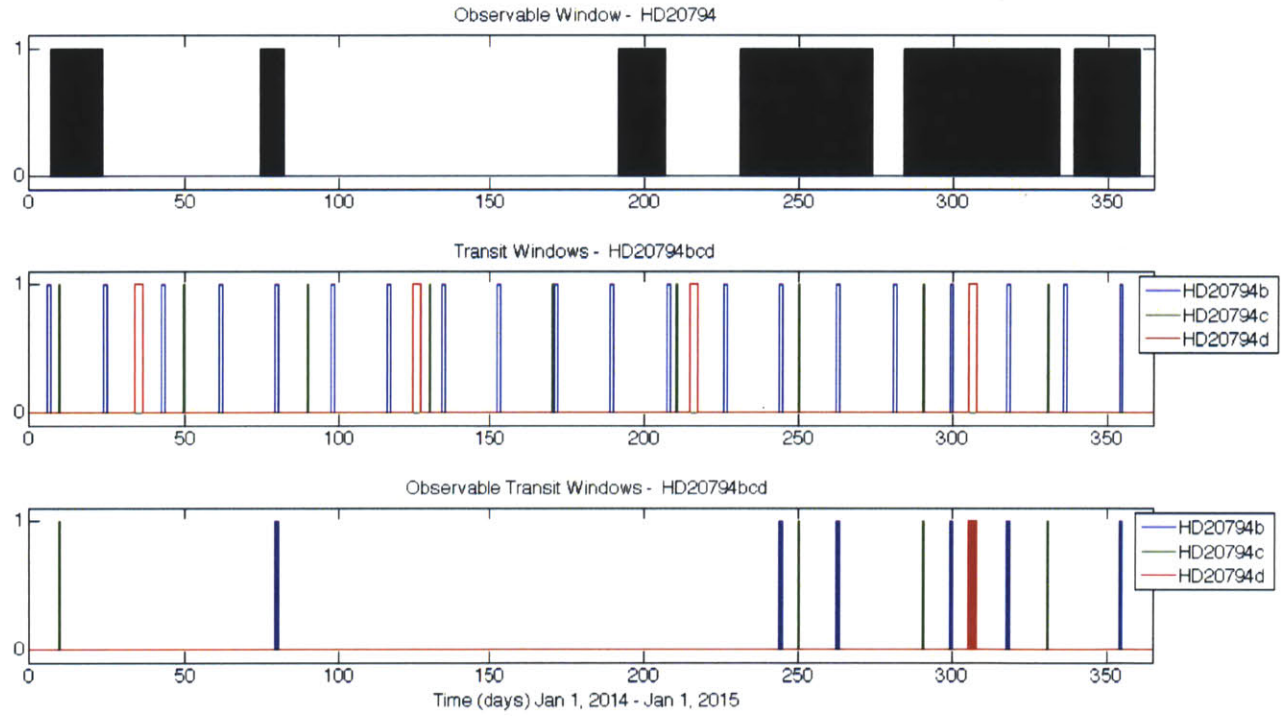

Figure 5-1: Predicted Transit, Observational, and Observational-Transit Windows for HD20794. Each point represents one minute. (Top) Observability of the star HD20794. A value of 1 indicates the star is visible to the satellite. What appears as fill on the observability graph is actually the constant switching of observability status, varying with orbit day and night. The data for the observable window was generated by Mary Knapp. (Middle) Transit Windows for HD20794b, HD20794c, and HD20794d. A value of 1 indicates the planet is transiting. (Bottom) Observable-Transit Windows for HD20794b, HD20794c, and HD20794d. A value of 1 indicates the star is observable and transiting. These windows were created by finding the overlap between the observable and transit windows.

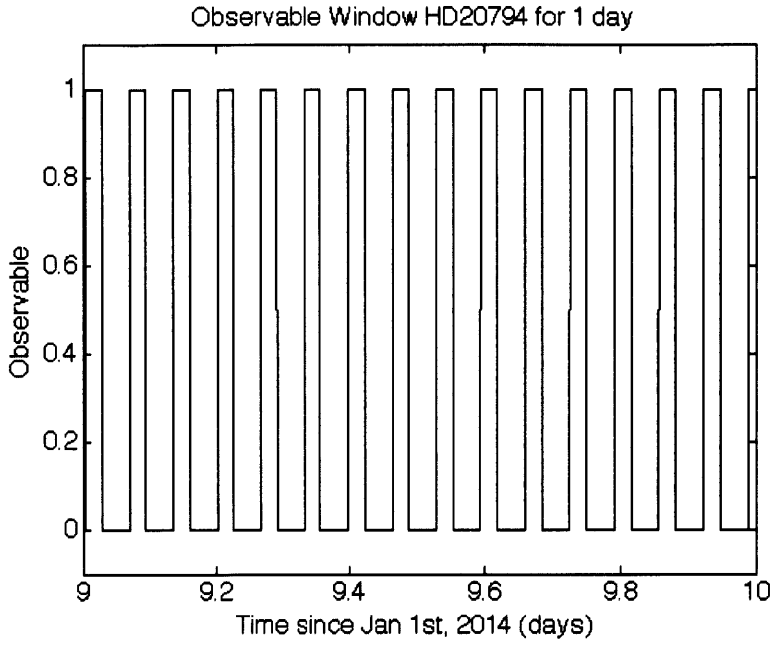

Figure 5-2: Observable Window Zoomed. The orbital day and night cycles are visible in each of the star's observable windows when zoomed in over a short period of time. When looking at the observable window over the year, this affect causes the graph to appear "filled in."

Table 5.2 gives a summary of the number of observable transits along with the properties for each target planet. Overall, eighteen out of the nineteen targets have at least one visible transit. In general, the planets with shorter periods have more observable transit windows than planets of longer periods.

Figure 5-3 shows all of the observable transit windows plotted together. At the start of the year, there is a high concentration of observable-transit windows but towards the end of the year there are gaps which last tens of days. These gaps are lowering the average visibility to approximately 0.1 over the course of the year, indicating that for 9 out of 10 minutes the satellite cannot observe because it is in orbit day or no transits are visible.[1] This inefficiency is mainly caused by an inability to observe any of the candidate stars over certain time periods because of the alignment of the Sun, Moon, and Earth. Thus, adding more potential candidates may not significantly raise the efficiency of the mission, because the new candidates

[1]The average visibility would be 0.22 if a transit was always available to observe when the satellite was ready (because it can only observe for 20 minutes during its 90-minute orbit).

Planet	Period (days)	Predicted Transit Window (hours)†	Num of Obs-Transit Windows
HD20794c	40.11	9.54	4
HD20794b	18.32	25.51	6
HD20794d	90.31	58.49	1
61Virb	4.22	32.75	32
HD102365b	122.10	536.80	1.5
muArac	9.64	23.92	17
HD136352b	11.58	5.35	13
HD136352d	106.72	69.89	2
HD136352c	27.58	10.51	6
55Cnce	0.74	0.06	52
HD69830b	8.67	6.38	16
HD69830c	31.56	139.70	6
HD189567b	14.28	3.89	10
HD134060b	3.27	1.42	48
HD96700b	8.13	3.14	18
HD96700c	103.49	33.77	1
HD1461b	5.77	3.45	24
HD134606b	12.08	3.89	12
HD134606c	59.52	31.56	0

Table 5.2: Observable-Transit Windows Summary.
† Predictions for the transit midtime and transit window length were made by Mary Knapp and Brice Demory and were based off of data from the Exoplanet Encyclopedia. [2]

would also not be observable during the gap times.

The maximum overlap of observable-transit windows is four, meaning four satellites would be needed to observe the entirety of every observable-transit window. However, once measurements have been taken during one observable-transit window, the planet can be determined to transit or not transit. If the planet does not transit, measurements do not need to be taken in future observable-transit windows. Therefore, the overlap of observable-transit windows may not cause a conflict in the observation plan.

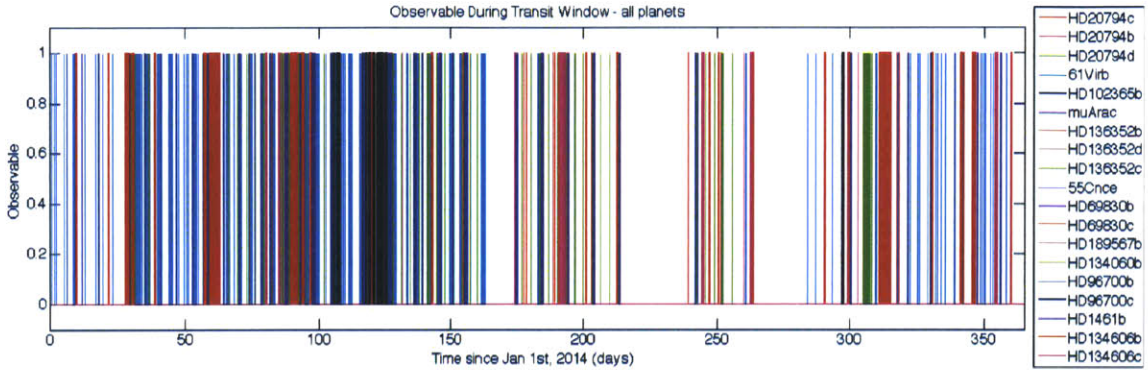

Figure 5-3: All Observable-Transit Windows. Eighteen out of Nineteen of the potential planets may have transits observable between one and fifty-two times. Several gaps lasting tens of days occur when no transits are visible.

5.2 Modeling Data of Transits Using the Results of the Frequency Study

Having an estimate for the amount of data which can be collected from the observable-transit windows allows a predicted set of light curves to be simulated for each planet.

With the exception of the planet's radius and orbital inclination angle, all of the properties necessary to define the light curve are known from the RV data of the planet. To estimate the planet radius, the planet selected for modeling was assumed to have the average density of perovskite ($MgSiO_3$), a mineral abundant in the Earth's mantle. Dividing the mass of the planet by this density produced an estimate for the

planet radius. The inclination angle can be estimated if the star's inclination angle, the angle between the star's rotational axis and the line of sight, is known. However, many stars' inclination angles are currently unmeasured, so the set of planets' orbital inclination angles were simulated to be at a value of 90°.

The predicted photometric data for HD20794c and HD20794d are shown in Figures 5-4 and 5-5 for a satellite with an optical system with an aperture size of 30-cm. While HD20794d can only be observed once, HD20794c can be observed up to four times. Because there are multiple windows to collect data for HD20794c, the light curve can be filled in over time.

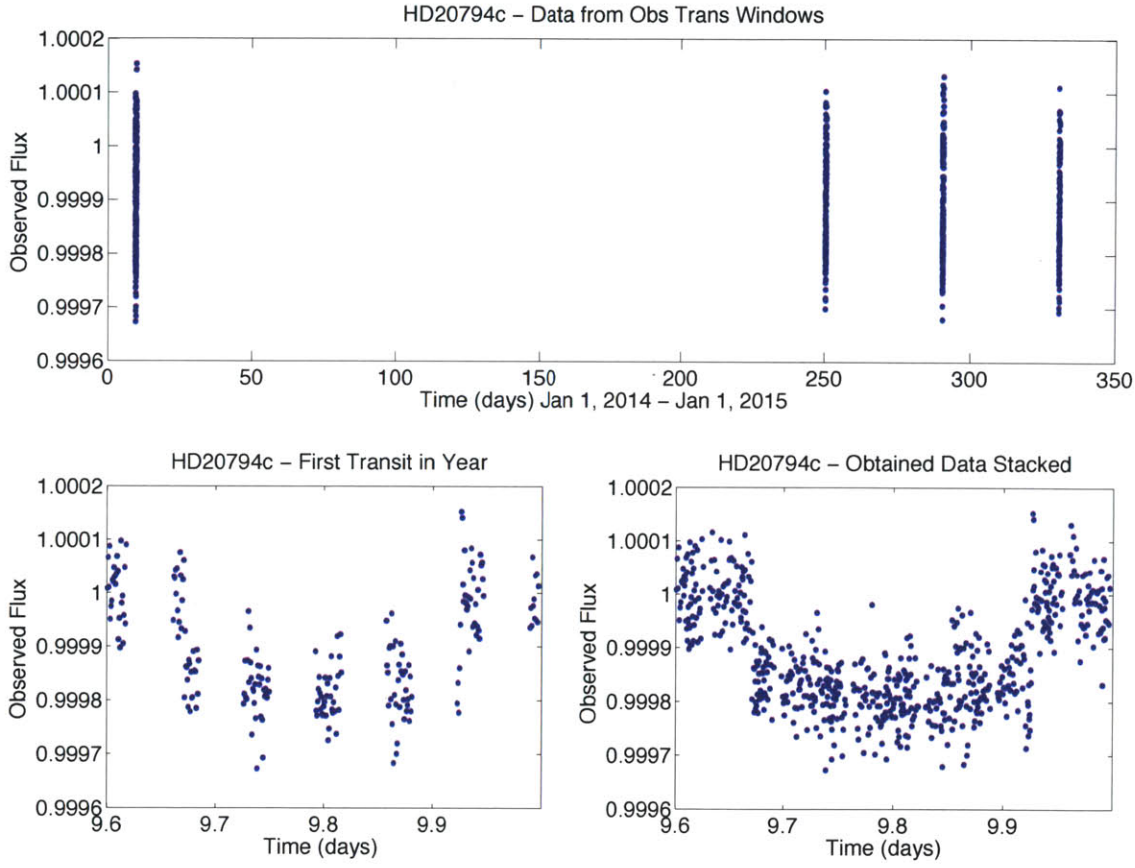

Figure 5-4: Data Collected from HD20794c Observational-Transit Windows. The three plots demonstrate the data which could be collected if HD20794c was observed during all of its observable-transit windows. Overall, four observable-transit windows are visible for HD20794c. By obtaining data during each window and stacking, the gaps can be filled. The data points are at a cadence of one minute, and an aperture size of 30-cm was assumed.

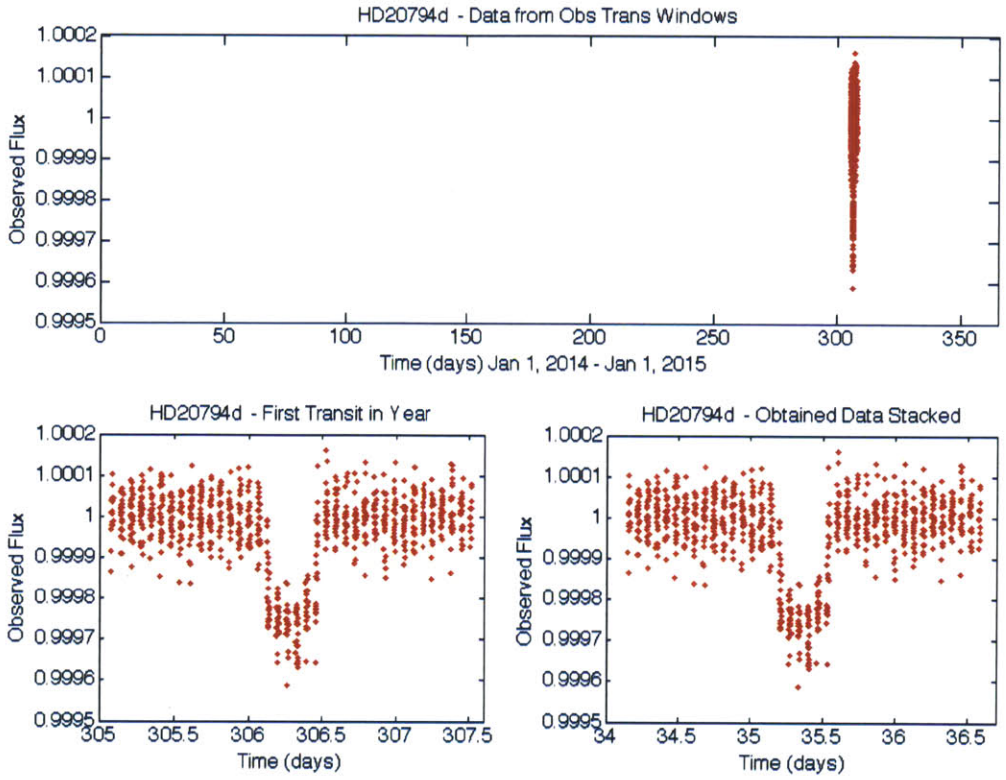

Figure 5-5: Data Collected from HD20794d Observational-Transit Windows. The three plots demonstrate the data which could be collected if HD20794d was observed during all of its observable-transit windows. Overall, one observable-transit window is visible for HD20794d, thus the graph of the data stacked is identical to that of the first transit. The data points are at a cadence of one minute, and an aperture size of 30-cm was assumed.

5.3 Probability of the Mission Measuring a Transit: ESPA Conditions Compared with ExoSat Conditions

5.3.1 Selecting Planets for a RV survey

To begin the selection of potential candidates, the entire list of known radial velocity planets from the Exoplanet Encyclopedia was considered [2].[2] From this list of 701

[2]Data from the Exoplanet Encyclopedia was retrieved on May 6th, 2012

planets, 230 planets already had a measured radius value To calculate the transit probability, the radius of the host star and the semi-major axis of the planet must be known, so planets which did not have these values listed in the Exoplanet Encyclopedia were also removed from the interest list. After these removals, 304 planets remained on the candidate list.

For each of these 304 planets, a calculation for the threshold of detection was made for a system which could be built in an ESPA satellite (30-cm aperture size with CCD detector) and ExoplanetSat (6-cm aperture size and CMOS detector). The theoretical minimum transit depth and photometric precision for which data could be taken were estimated for each planet in order to calculate the threshold of detection.

In order to evaluate the minimum transit depth, a minimum radius value was estimated by applying the the mass-radius relationship for a planet made out of pure iron (model created by Seager et. al. 2007) [27]. This relationship accounted for the varying density of iron inside a planet due to pressure from gravitational forces. Although each planet is likely to contain minerals that are not iron, assuming that the planet is made of pure iron will yield the most conservative estimate for the transit depth.

The photometric precision was estimated by applying the noise budget described in Chapter 3 for two cases: 30-cm aperture size with a CCD detector (ESPA) and a 6-cm aperture size with a CMOS detector (ExoSat). An observational cadence of 20 minutes was used, which represents the amount of data which could be collected in one orbit night.

Dividing the minimum transit depth by the photometric precision yielded an estimate for the detection threshold which could be achieved in one orbit night. Planets which could be detected to greater than 7σ were put onto the "7σ-detection list" for each platform. By using the ESPA parameters, 241 planets could be detected to a level of 7σ, while only 27 planets could be detected to this level using ExoSat. If 7σ were used as the determining detection threshold for choosing candidates, the number of potential targets for a satellite with the ESPA parameters would be 9 times larger than ExoplanetSat's potential targets.

In addition to having more targets, the ESPA satellite's 7σ-detection list contains planets with transits requiring a higher level precision to measure. The planets requiring the highest level of photometric precision cannot be measured by ground surveys or current space missions, so they would be valuable targets for an ESPA-class satellite mission.

A full list of the 304 candidate planets with their estimated radius, photometric precision values, and detection thresholds are listed in Appendix A.

5.3.2 Probability of Discovering Transits of Known-RV Planets

The proper alignment of the observer, planet, and star is needed for a transit to happen; thus, each planet has a small chance of transiting. The probability for each candidate planet on the known RV list was calculated using Equation 1.3 from Chapter 1 (listed in Appendix A). These calculated probabilities only depend upon the geometry of the star system and do not depend on previously measured values for the star's spin inclination angle or the orbital inclination angle measured for other planets in the system.

The probability distributions for finding a given number of planets to transit were found using the 7σ-detection list for the ESPA condition (30-cm aperture size with CCD detector) and ExoplanetSat condition (6-cm aperture size and CMOS detector). The probability distributions for finding the exact number of transits which can be measured by a mission were Gaussian in form (Figure 5-6a). Overall, the 7σ-detection list for the ESPA condition is most likely to yield a discovery of six transiting planets, while the 7σ-detection list for ExoSat is most likely to find zero planets.[3] The distribution for the ESPA probabilities was wider than the distribution for the ExoSat probabilities ($\sigma_{ESPA} = 2.4 > \sigma_{ExoSat} = 1.6$).

The probability of detecting "at least" a given number of transits was also calculated (Figure 5-6b). While the prospects for detecting at least one planet that transits

[3]The actual mean for the Gaussian fit to the ExoSat distribution was 0.22, which when rounded to the nearest planet is zero.

Platform	Aperture Size	Detector	# RV planets can target†	Most probable # of transits to detect	Prob at least 1 transit	Prob at least 5 transit
ESPA	30-cm	CCD	241	6± 2.4	99.9%	75.1%
ExoSat	6-cm	CMOS	27	0±1.2	54.2%	0.05%

Table 5.3: Summary of the Probability of Discovering a Transit: ESPA versus ExoSat. †This is the number of known RV planets (with the stellar radius and semi-major axis listed in the Exoplanet Encyclopedia) that have transits which could be detected to a 7σ value in 20 minutes of data

was near 100% if a mission were to monitor all the planets on the ESPA 7σ-detection list, the likelihood of finding at least one transit from the ExoSat list was only 54%. Both missions have a near zero probability of detecting more than 15 transits.

Table 5.3 gives an overall summary of the expected transit haul from both the ESPA and ExoplanetSat 7σ-detection list.

The probability estimates in this chapter likely represent a lower bound for the number of transits that could be found, because additional planets could be measured to 7σ if the observational cadence duration were increased to longer than 20 minutes. Planets with transit durations longer than 180 minutes (two orbital periods of the satellite) will overlap with two orbit nights and so the observational cadence could potentially be increased. The candidate list could also be expanded if the semi-major axis and/or the stellar radius were determined for planets which were removed because of missing data.

Despite the potential of adding planets to the candidate list, it is possible other RV-followup surveys have investigated planets on this candidate list and determined that they do not transit. In this case, planets would be removed from the list, and the overall probability of finding a transit would decrease.

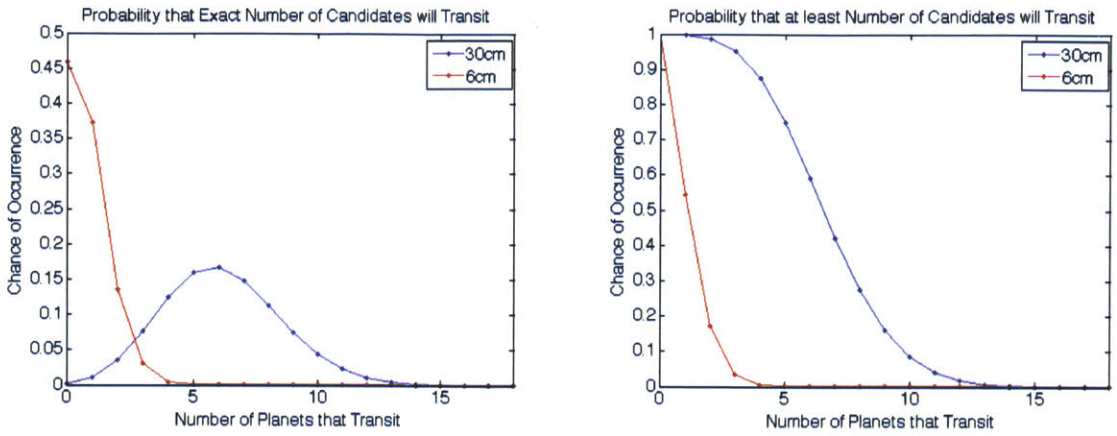

(a) Probability of the Exact Number of Candidates that will Transit.

(b) Probability that at Least the Number of Candidates will Transit.

Figure 5-6: Probability of Candidates Transiting. Unfortunately, it is not probable that every planet on the target list will transit. By monitoring the target list for the 30-cm aperture size with the CCD detector (blue), the mission has the highest probability of detecting six transits. Using the target list for the ExoSat conditions (red), the mission has the highest probability of finding no transits. For a 30-cm aperture size with the CCD detector, there is a near 100% chance of detecting at least one transit (blue) while the ExoSat condition target list has only a 54% chance of yielding one transit (red). The probabilities for the transit of each planet were based purely on the geometric alignment of the system.

5.4 Beyond RV follow-up: Expected Results of a Transit Survey using a Mid-sized Nanosatellite around G and K stars

Beyond performing RV-followup studies, nanosatellites could be used to complete space-based transit surveys around bright stars. In a transit survey, stars which do not have known planets would be continuously monitored to search for dips in their brightness.

5.4.1 Number of Non-variable G and K Stars which could be Monitored

The results of the total noise budget calculations allow us to set a constraint on the brightness of the stars which could be monitored to find a transit of an Earth-sized

planet (Figure 5-7). Having a cutoff for the dimmest magnitude with the allowable photometric precision to detect an Earth-sized planet allows us to find the number of potential target stars available for monitoring if a general transit survey were performed (Figure 5-8). Estimates were found for the number of potential targets for such a transit survey by searching for non-variable G and K type stars in the *Hipparcos* catalog that were brighter than photometric precision cutoff. The expected results of this search are listed in Tables 5.4 and 5.5.

As the aperture size increased and the magnitude limit became dimmer, more stars were within the photometric precision limit for detecting an Earth-sized planetary transit to a 7σ detection threshold. For a one-hour and a three-hour observational cadence, the number of stars for monitoring increased more than two orders of magnitude as the aperture size was increased from 5-cm to 40-cm.

In order to monitor this many stars with an observational cadence of one hour or more, many satellites working together would be required.

Apt Size (cm)	Mag limit, 1hr	Num stars in Hip†	Expected # planets to find at 1AU††	Mag limit, 3hr	Num stars in Hip†	Expected # planets to find at 1AU††
5	3.2	2	0	4.7	12	0
10	4.8	13	0	6.2	108	1
15	5.7	49	0	7.1	343	2
20	6.3	123	1	7.8	793	4
25	6.8	212	1	8.2	1248	6
30	7.2	388	2	8.6	2002	9
35	7.5	541	3	9	2977	14
40	7.8	793	4	9.3	3801	18

Table 5.4: CCD - Magnitude Limit to Detect Earth-Sized Planets for Different Apertures.
† The number of non-variable G and K type stars listed in the *Hipparcos Star Catalog* that are brighter the the magnitude limit for a 7σ detection in the given period of time.
†† Found using the number of *Hipparcos* stars. The assumption was used that all stars would have a planet at 1AU (giving the upper bound for the estimate for planets found). The average star radii was assumed to be equal to the radius of the sun.

Apt Size (cm)	Mag Limit, 1hr	Num Stars in Hip†	Expected # planets to find at 1AU††	Mag Limit, 3hr	Num Stars in Hip†	Expected # planets to find at 1AU††
5	2.8	2	0	4.2	5	0
10	4.3	8	0	5.7	49	0
15	5.1	22	0	6.6	202	1
20	5.8	59	0	7.2	388	2
25	6.3	123	1	7.7	702	3
30	6.7	226	1	8.1	1117	5
35	7	311	1	8.4	1586	7
40	7.3	431	2	8.7	2213	10

Table 5.5: CMOS - Magnitude Limit to Detect Earth-Sized Planets for Different Apertures.
† The number of non-variable G and K type stars listed in the *Hipparcos Star Catalog* that are brighter the the magnitude limit for a 7σ detection in the given period of time.
†† Found using the number of *Hipparcos* stars. The assumption was used that all stars would have a planet at 1AU (giving the upper bound for the estimate for planets found). The average star radii was assumed to be equal to the radius of the sun.

5.4.2 Expected Number of Planets to Discover in a Transit Survey Using a Mid-sized Nanosatellite

Upper-bound estimates were made for the expected number of planets which could be found in a transit survey by using the values for the number of stars which could be monitored. Every star was assumed to have a planet at the semi-major axis of interest, and the group of *Hipparcos* stars at each aperture size were assumed to have an average stellar radius equal to the sun.

Figure 5-9 shows the number of planets that would be expected to be found orbiting at 1AU if all stars from the *Hipparcos* list could monitored. For the cases evaluated, between zero and 18 planets have the probability of being discovered to orbit at 1 AU given the size of the candidate list at each aperture. At least one planet could be expected to be found if all stars were monitored from the lists using aperture sizes of 25-cm and larger.

Figure 5-10 shows the expected planet haul at 1AU compared to the planet haul at 0.5AU and 0.05AU. Because planets which orbit close to their stars have a high

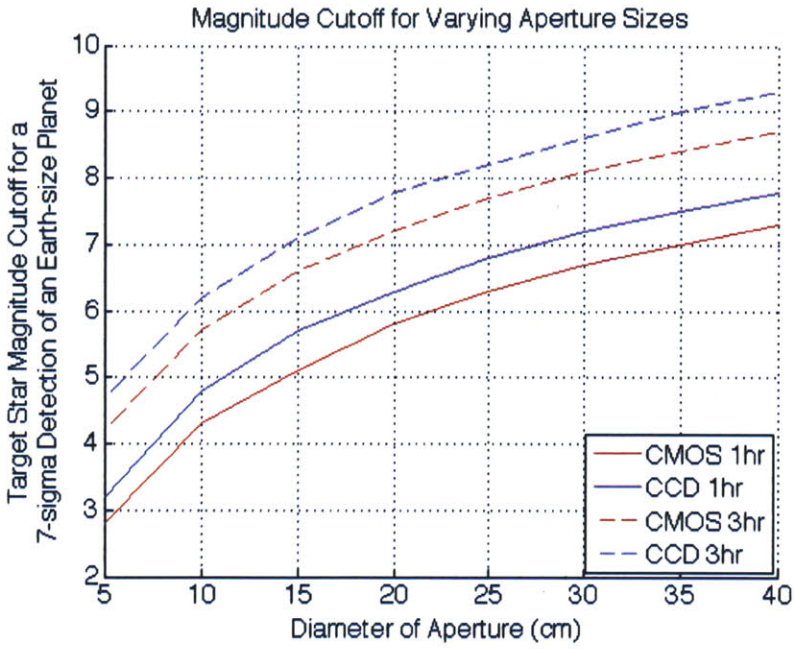

Figure 5-7: Magnitude Cutoff Varying by Aperture Size. The "magnitude cutoff" represents the dimmest target star magnitude in which an Earth-sized planet transit can be detected to a 7σ value. The time resolutions stated represent the amount of data taken and not actual time that has passed. For example, one hour indicates three orbit nights which is 4.5 hours of actual time that has passed. The CMOS detector (red) has brighter magnitude cutoffs than the CCD detector (blue).

probability of being detected by the transit method, the plot of the excepted number of planets found at 0.05AU represents the maximum number of planetary systems which could be found given each number of candidate stars.

5.4.3 Transit-Survey Mission Lifetime Requirement

To declare a detection using the transit method, the transit of a planet must be measured three times. Because of this requirement, the lifetime for a transit survey mission must be at least 3 times the orbital period of the target planets. Assuming that the first transit will not be measured on day one of the mission, it is possible that the scanning time must be up to four times the orbital period of the target planet in order to measure three transits (3 Periods $< T_{lifetime} <$4 Periods). To find a planet with an orbital period equivalent to Earth's orbital period, the mission

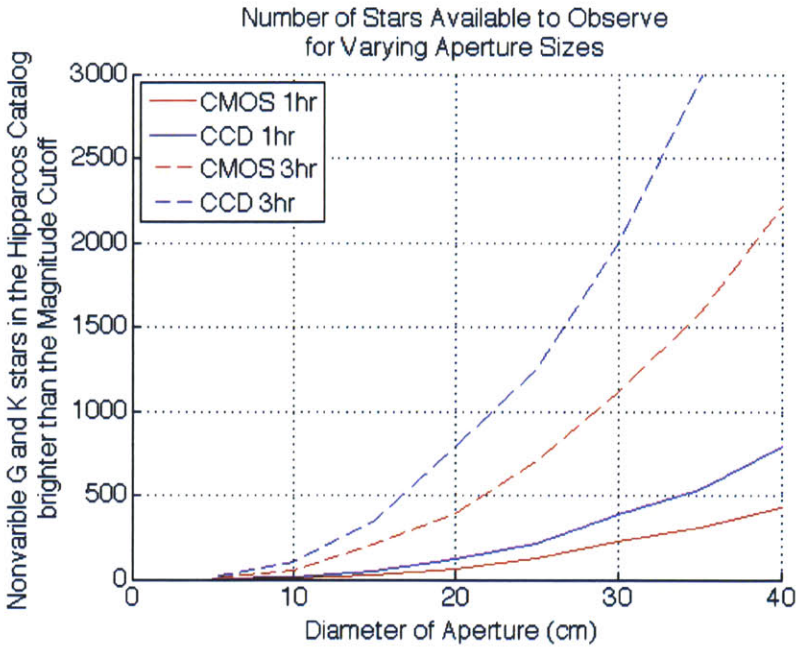

Figure 5-8: Number of Stars Available to Observe Varying by Aperture Size. The number of stars available to observe were found by searching the *Hipparcos Star Catalog* for Non-variable G and K type stars that were brighter than the magnitude cutoff at each aperture sizes. The time resolutions stated represent the amount of data taken and not actual time that has passed. For example, one hour indicates three orbit nights which is 4.5 hours of actual time that has passed. By using the CCD detector (blue) as oppose to the CMOS detector (red), more stars are eligible to be observed given the same aperture size.

lifetime requirement must be four years.

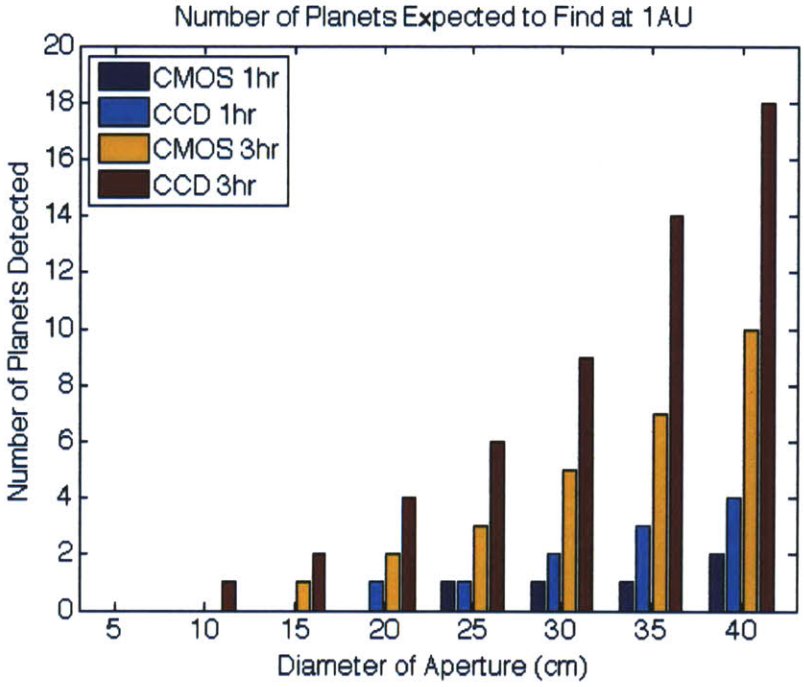

Figure 5-9: Upper-Bound Estimate for the Number of Planets Expected to Find Orbiting at 1AU. Given the number of G and K type targets which could be monitored for a transit survey under each condition, the expected number of planets orbiting at 1AU were calculated. Estimates were made using the assumption that every star had a planet orbiting at 1AU.

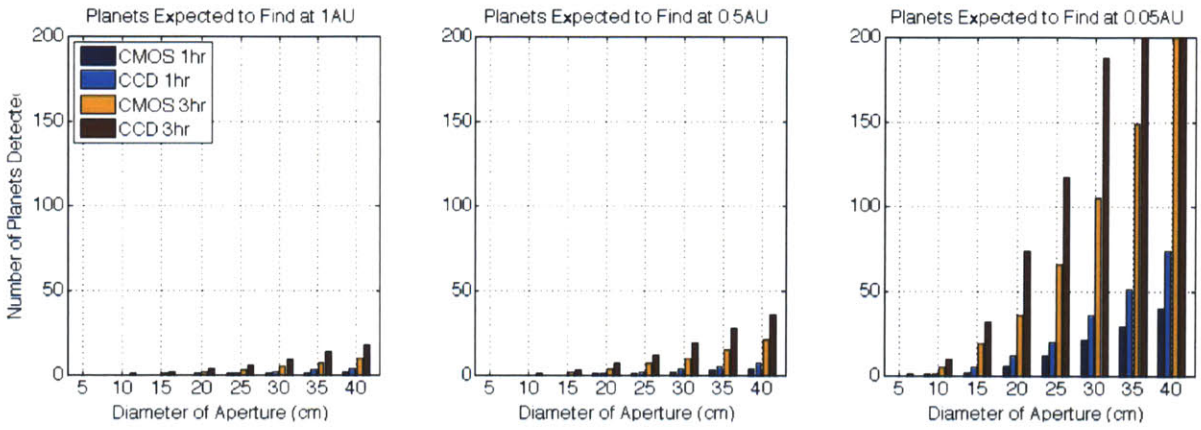

Figure 5-10: Upper-Bound Estimates for the Number of Planets Expected to Discover Orbiting at 1AU, 0.5AU, and 0.05AUs. These estimates were made assuming that every star had a planet orbiting at a given semi-major axis, in order to produce an upper-bound estimate for the number of planets which could be found. More planets are expected to be found that orbit at a small semi-major axis. Because planets which orbit close to their stars have a high probability of being detect by the transit method, the plot of the excepted number of planets found at 0.05AU represents the maximum number of planetary systems which could be given each number of candidate stars.

Chapter 6

Discussions and Recommendations Related to the Future Use of Mid-sized Nanosatellites to Measurements of Exoplanets

6.1 Size Limiting Factors for Building Satellites to Perform Photometry

In order to design a system in a small satellite which is capable of collecting photometric data with the best precision possible, it is critical to minimize the shot noise, jitter noise, and noise due to the gain drift.

If improving the photometric precision over a short period of time (under one orbital night) is paramount, then reduction of the jitter noise is more important than reduction of the shot noise. This would be necessary to monitor planets with small semi-major axes. In contrast, when observing dim target stars for long observation periods, it is important to focus on reducing the shot noise. Reducing the shot noise is more critical for monitoring planets with a large semi-major axes. If the planet hunting focuses on observing planets with a similar period to Earth, it is more

important to reduce the shot noise.

In a third scenario, the noise from the gain drift has the potential to dominate the shot and the jitter noise if the temperature of the detector is unmitigated. The noise due to gain drift is unrelated to target star choice and length of observation, so there is no way to improve this value by choosing another target star or collecting data over a longer period of time.

Listed below are strategies designers should consider for minimizing each of these noise sources:

Jitter

(A) Reduce the jitter amplitude by improving pointing control

(B) Choose a detector with small intra-pixel variation.

Shot

(C) Maximize the size of the aperture

(D) Use a detector with a better quantum efficiency[1]

Gain Drift

(E) Control the nonsystematic variations in the detector's temperature

While observing most target stars, the shot noise will be the limiting noise source, so implementing Strategies C and D are the most crucial. Performing Strategy C (maximize the size of the aperture) is essential because the photon arrival rate scales linearly with the aperture area (Equation 3.2).

Unfortunately, Strategy C is the most sensitive to the size of the satellite platform. Other strategies for reducing the total noise could be accomplished in a smaller frame by downsizing the size of components, such as building a smaller temperature control device (Strategy E), or by upgrading the detector chip (Strategies B and D). However, there is no way to reduce the size of the collection area and still collect the same number of photons from a given star.

[1]The difference in readout rates between the CCD and CMOS detectors was not a significant factor.

Strategy A (reduce the jitter amplitude) is also related to the size of the spacecraft, but it is dependent on the mass and not the volume of the platform. Adding more mass to the spacecraft increases the satellite's moment of inertia making the spacecraft harder to displace, and thus decreasing the jitter amplitude.

6.2 Constellation of CubeSats verses One ESPA-Class Satellite

Although larger satellites provide more space for building a system to perform photometry with higher precision, large satellites also cost more to construct and launch. The total cost estimate for ExoplanetSat (3U CubeSat) is about $500,000, while the cost of repurposing the ESPA-spacecraft Castor for use in performing astronomical photometry is roughly $10 million [28]. Given the cost constraint of $10 million, approximately 20 ExoSats could be commissioned whereas only one ESPA-class satellite could be designed and launched.

6.2.1 Advantages of a Constellation of CubeSats

A satellite constellation – a group of satellites working together to accomplish one goal – could be used to improve the coverage of targets, increasing the amount of data collected and providing a more constant dispersion of measurements over time. By using satellites dispersed amongst different low Earth orbit configurations, stars which are not visible for part of the year to one satellite can be monitored by others in the constellation.

Because many satellites are needed to constantly monitor stars, a constellation of CubeSat is better suited for performing transit survey than one larger satellite. If observation during the entirety of orbital night were possible, three satellites could monitor the entirety of a transit continuously. If observations can only take place for 20 minutes every orbit night, five satellites are needed for complete coverage. Thus, 20 satellites could potentially monitor at least four target stars continuously. The

best one satellite could do would be to monitor one star with hour long gaps in the data set, or it could monitor several stars with very long gaps in coverage.

Although a constellation of satellites can provide greater coverage, the extra spacecraft will be useless unless there are a significant number of targets. Recalling the results of the transit survey case study (discussed in Section 5.4), only 2 non-variable G and K type stars could be monitored to potentially find a transiting planet as small as Earth. With so few targets, having extra coverage is not an advantage; thus, the target list must be expanded. To bolster the number of stars to be monitored, either the standard of detection must be lowered to a value which is smaller than 7σ or the mission would be limited to finding planets which are larger than Earth-sized.

Even though this type of survey using CubeSats may not have the ability to detect an Earth analog, finding solar systems containing larger planets may eventually lead to the discovery of smaller planets. Planets that orbit around the same star tend to lie in the same orbital plane, meaning that if one planet is detectible by transit, other planets in the system may be detectable. Returning to those solar systems with a more sensitive instrument may reveal other transiting planets.

Choosing to launch many satellites instead of one also provides redundancy. If one satellite in a constellation is lost or damaged, the constellation as a whole can still function. Similarly, satellites could be removed from the constellation in order to lower the total mission cost. This way, the budgets of CubeSat constellation missions could remain flexible.

6.2.2 Advantages of Using One ESPA-Class Satellite

Although there is a cost benefit for using CubeSats, ESPA-class satellites can perform measurements which a constellation of smaller satellites cannot. The CubeSat platform severely limits the aperture area of the optical system. For the same cost, the aperture area available in one ESPA-class satellite is larger than the combination of many ExoSat units. For example, one satellite containing an optical system with an aperture diameter of 30-cm would be equivalent to 25 ExoSats in aperture area (Figure 6-1). A 30-cm aperture is a conservative estimate for what would fit inside an

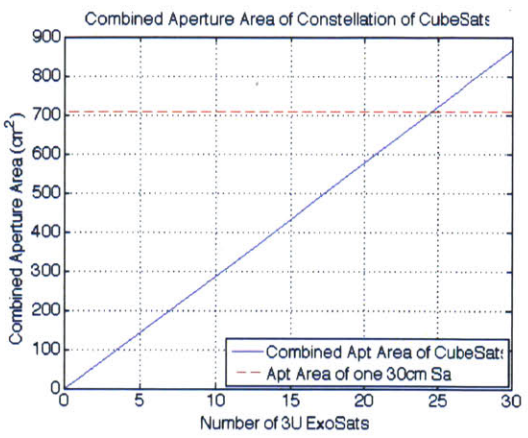

(a) Combined Aperture Area of many ExoSats

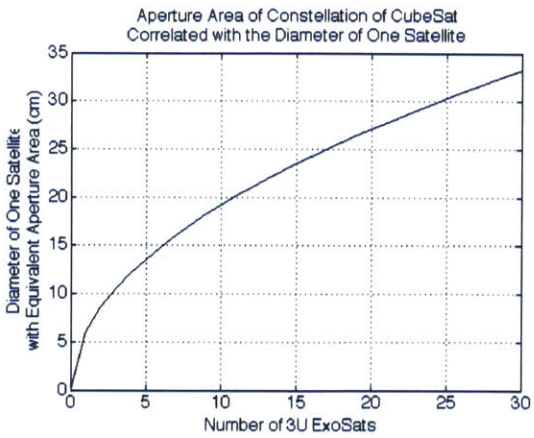

(b) One Satellite Equivalent-Area Aperture Diameter for varying ExoSats

Figure 6-1: Aperture Area of a Constellation of ExoplanetSats. (left) The total aperture area of the combining 3U ExoSat vehicles increase linearly as more satellites are added. The aperture area for a 30-cm diameter aperture is approximately equivalent to the aperture area of 25 ExoSats combined. (right) The number of ExoSat units which must be combined to reach the equivalent aperture area for one satellite with a larger diameter aperture.

ESPA satellite, while 25 ExoSats would cost approximately $12.5 million, exceeding the limit of $10 million.

Because one-satellite contains a larger aperture area, more photons could be collected from a given target in the same amount of time. Therefore, the shot noise in the data set would be lower, and the one ESPA satellite could reach a higher photometric precision value than a constellation containing 20 ExoSats all pointing at the same object. In addition, processing the data would be easier because the random photon noise would be smaller, hence making it easier to characterize the systematic errors in the data set. Due to these factors, the ESPA satellite is the suggested choice for detecting small planets which require high levels of photometric precision.

One ESPA satellite is well suited for performing an RV followup mission because RV followup missions demand significantly less coverage than a transit survey mission. RV followup measurements are predicted to occur in small windows of time, so many stars can be monitored for short periods of time in one mission.

Bibliography

[1] Smith, Matthew W. et al. ExoplanetSat: detecting transiting exoplanets using a low-cost CubeSat platform. Space Telescopes and Instrumentation 2010: Optical, Infrared, and Millimeter Wave. Ed. Jacobus M. Oschmann et al. San Diego, California, USA: SPIE, 2010. 773127-14.

[2] *The Extrasolar Planets Encyclopedia*, accessed at *http://exoplanet.eu/* March, 2012.

[3] Haswell, Carole. *Transiting Exoplanets.* Cambridge, United Kingdom: Cambridge University Press, 2010.

[4] Bevington, Philip and Keith Robinson. *Data Reduction and Error Analysis for the Physical Sciences.* New York, NY: McGraw-Hill, 2003.

[5] Silva-Valio, Adriana. *Estimating Stellar Rotation from Starspot Detection During Planetary Transits. The Astrophysical Journal*, 683: L179L182, 2008 August 20.

[6] Townsend, Rich (27 January 2003). *The Search for Extrasolar Planets (Lecture).* Department of Physics & Astronomy, Astrophysics Group, University College, London.

[7] Thakker, Purvesh and Wayne Shiroma. *Emergence of Pico- and Nanosatellites for Atmospheric Research and Technology Testing.* Reston, Va. : American Institute of Aeronautics and Astronautics, 2010.

[8] Bearden, David. "Small-Satellite Costs," *Crosslink* 2001. Accessed at *http://www.aero.org/publications/crosslink/winter2001/04.html* on March 13th, 2012.

[9] Moranta, Sebastien. *Small Launchers for Small Satellite: Launch Events Trends and Perspective - a Quantitative Analysis Based on Historical Trends (1988-2010)*, IAC-11.B4.5.1, 2011.

[10] "CubeSat Design Specification Rev. 12". California State Polytechnic University.

[11] Pumpkin CubeSat Kit. Accessed at *http* : *//www.cubesatkit.com/*, April, 2012.

[12] NASA. *GeneSat-1*, accessed at *http* : *//www.nasa.gov/centers/ames/missions/*2007/*genesat*1 3/26/07.

[13] NASA. *PharmaSat Mission Update*, accessed at *http* : *//www.nasa.gov/centers/ames/news/features/*2009/*pharmasat* − $update_0$612.*html*, 6/12/09.

[14] *QuakeSat Mission*, accessed at *http* : *//www.quakefinder.com/services/quakesat*− $ssite/qs_m ission.htm$, 6/6/04.

[15] Christopher M. Pong, Sungyung Lim, Matthew W. Smith, David W. Miller, Jesus S. Villaseor and Sara Seager, "Achieving high- precision pointing on ExoplanetSat: initial feasibility analysis", Proc. SPIE 7731, 77311V (2010); doi:10.1117/12.857992.

[16] *DoD Space Test Program Secondary Payload Planners Guide For Use On The EELV Secondary Payload Adapter*, version 1.0. Accessed at *www.everyspec.com* on Jan 9th, 2012.

[17] *ESPA The EELV Secondary Payload Adapter.* Accessed at *http* : *//www.moog.com/literature/*$Space_D efense/Vibration_C ontrol/MoogCSA_E SPA$0710.*pdf*, March 2012.

[18] Tompkins, Paul D.; Hunt, Rusty; D'Ortenzio, Matt D.; Strong, James; Galal, Ken; Bresina, John L.; Foreman, Darin; Barber, Robert; Shirley, Mark; Munger, James; Drucker, Eric. *Flight Operations for the LCROSS Lunar Impactor Mission.* NASA. Ames Research Center.

[19] Peters, E. *CASTOR Satellite Design Document,* November 18, 2010, page 194.

[20] Cyperus HAS-2 Detailed Specification - ICD.

[21] Lincoln Labs CCID41 Specification Sheet.

[22] Li, Luyao. *Millikelvin Temperature Control System for the ExoplanetSat Imager.* Masters Thesis, Massachusetts Institute of Technology, Cambridge, 2010.

[23] Chromey, Frederick. *To Measure the Sky: An Introduction to Observational Astronomy.* Cambridge University Press, New York NY, 2010.

[24] Jensen-Clem, Becky. *ExoplanetSat Design Doc Spring 2011*, p 33-37.

[25] Smith, Matt. *Error Budget* excel file and Personal Conversations between July, 2011 and March , 2012.

[26] Bernard Widrow and Istvn Kollr, "Quantization Noise: Roundoff Error in Digital Computation, Signal Processing, Control, and Communications," Cambridge University Press, Cambridge, UK, 2008. 778 p. ISBN-13: 9780521886710, ISBN: 0521886716

[27] Elkins-Tanton, Linda and Sara Seager, "Ranges of Atmospheric Mass and Composition of Super-Earth Exoplanets," The Astrophysical Journal, 685:1237Y1246, 2008 October 1.

[28] Knapp, Mary. Personal Conversations between April 14th, 2012 and May 14th, 2012.

Appendix A

Summary of Planet Candidates Used in Determining the Probability of Discovering a Transit in an RV Followup Mission

The properties of the 306 planets used for the probability study in Section 5.3.2 are listed in the following table by increasing sigma of detectability for 30-cm. The planets which do not have detectable transits are listed at the top of the table. The photometric precision values listed are for an observational cadence of 20 minutes.

Planet Name	Star Vmag	ppm 30-cm CCD	ppm 6-cm CMOS	Planet Mass (M_{Jup})	Predicted Fe Radius (R_{Earth})	Transit Depth (ppm)	σ detection using 30-cm	σ detection using 6-cm	Prob of Trans (%)
11 Com b	4.74	12.4	37.2	19.4	0.89	9.1	0.73	0.24	6.85
HD 13189 b	7.57	23.2	141.2	14	2.09	18.22	0.79	0.13	12.67
CoRoT-7 c	11.7	143.8	2539.2	0.0264	1.1	117.98	0.82	0.05	8.9
HD 99706 b	7.81	25.4	159.8	1.4	1.18	39.82	1.57	0.25	1.18
HD 96167 b	8.09	28.3	186.2	0.68	0.97	45.78	1.62	0.25	0.67
HAT-P-13 c	10.62	85.3	1028.7	14.5	1.65	154.35	1.81	0.15	0.62
81 Cet b	5.65	14	55.5	5.3	1.36	26.97	1.93	0.49	2.05
HD 110014 b	4.66	12.4	35.9	11.09	1.3	30.35	2.46	0.84	4.54
HD 102329 b	8.04	27.7	181.1	5.9	1.76	68.22	2.46	0.38	1.46
HD 180902 b	7.78	25.1	156.7	1.6	1.31	62.43	2.49	0.4	1.38
eps Tau b	3.53	11.6	28.5	7.6	1.58	28.9	2.49	1.01	3.3
BD-103166b	10.08	66.5	676.8	0.48	1.42	173.42	2.61	0.26	17.41
HD 210277 b	6.63	17.3	87.8	1.23	0.8	45.28	2.62	0.52	0.47
HD 206610 b	8.34	31.2	214.6	2.2	1.62	90.82	2.91	0.42	1.69
HD 108147 b	6.99	19.2	104.8	0.261	0.98	56.49	2.94	0.54	5.6
HD 142245 b	7.63	23.8	145.2	1.9	1.54	70.11	2.95	0.48	0.88
HD 102272 c	8.71	36.3	266.5	2.6	2.18	110.84	3.05	0.42	3
HD 102272 b	8.71	36.3	266.5	5.9	2.2	112.79	3.11	0.42	7.66
HD 180314 b	6.61	17.2	88.2	22	2.08	54.06	3.14	0.61	3.06
HD 102956 b	8	27.3	177.2	0.96	1.71	87.59	3.21	0.49	25.34
HD 8673 b	7.57	23.2	141.2	14.2	1.24	74.85	3.23	0.53	0.24

HD 28678 b	8.54	33.9	241.2	1.7	2.01	112.4	3.32	0.47	2.33
HD 212771 b	7.6	23.5	142.9	2.3	1.12	79.37	3.38	0.56	1.91
BD-17 63 b	9.62	54	484.6	5.1	1.11	188.1	3.49	0.39	0.24
HD 4313 b	7.83	25.5	161.3	2.3	1.78	90.11	3.53	0.56	1.92
11 UMi b	5.02	12.8	43.4	10.5	1.34	46.93	3.67	1.08	7.27
HD 38801 b	8.26	30.2	204.9	10.7	1.58	113.9	3.77	0.56	0.7
HD 125612 c	8.31	30.8	211	0.058	1.33	123.03	3.99	0.58	9.88
HD 100655 b	6.45	16.5	80.5	1.7	2.13	66.46	4.03	0.83	5.7
HD 5891 b	8.25	30.1	203.8	7.6	2.4	132.87	4.42	0.65	5.34
HD 200964 c	6.64	17.3	88.2	0.9	1.39	77.83	4.49	0.88	1.03
HD 181342 b	7.55	23.1	139.2	3.3	2.07	106.88	4.63	0.77	1.21
14 And b	5.22	13.1	45.8	4.8	1.89	62.01	4.73	1.35	6.17
HD 86081 b	8.73	36.6	270.4	1.5	1.76	177.46	4.84	0.66	14.74
HD 108863 b	7.89	26.2	166.8	2.6	2.29	129.1	4.93	0.77	1.87
HD 240237 b	8.19	29.4	197	5.3	2.25	148.81	5.06	0.76	7.84
ups And d	4.09	11.9	28.5	10.19	1.1	62.85	5.29	2.21	0.3
HD 11977 b	4.7	12.4	36.6	6.54	1.69	65.69	5.3	1.8	3.14
HD 175541 b	8.03	27.6	180.1	0.61	2.18	146.42	5.31	0.81	1.75
HD 50499 b	7.22	20.6	117.5	1.71	1.45	110.18	5.34	0.94	0.17
HD 106270 b	7.73	24.7	152.7	11	1.66	132.21	5.35	0.87	0.27
HD 1502 b	8.52	33.6	238.3	3.1	2.39	185.1	5.51	0.78	1.6
HD 224693 b	8.23	29.9	201.5	0.71	1.86	164.75	5.52	0.82	3.43
HD 131496 b	7.96	26.9	173.3	2.2	2.19	155.68	5.79	0.9	1.03
HD 8574 b	7.12	20	111.8	2.11	1.39	118.75	5.94	1.06	0.83
HD 34445 b	7.31	21.3	123	0.79	1.31	126.25	5.94	1.03	0.31
HD 33283 b	8.05	27.8	182.1	0.33	1.76	168.97	6.08	0.93	3.37
24 Sex c	7.38	21.8	127.5	0.86	1.94	133.62	6.14	1.05	1.1
HD 33142 b	8.13	28.7	190.4	1.3	2.14	176.34	6.14	0.93	1.85
HD 95089 b	7.92	26.5	169.6	1.2	2.2	163.11	6.16	0.96	1.51
HD 18742 b	7.97	27	174.3	2.7	2.26	168.06	6.23	0.96	1.19
HD 116029 b	8.04	27.7	181.1	2.1	2.28	174.67	6.3	0.96	1.24
18 Del b	5.52	13.7	57	10.3	2.36	88.54	6.46	1.55	1.52
HD 216435 b	6.03	15	66.1	1.26	1.4	97.45	6.5	1.47	0.37
ksi Aql b	4.72	12.4	37.2	2.8	2.17	81.81	6.6	2.2	8.22
HD 204941 b	8.45	32.6	228.7	0.266	1.18	215.31	6.6	0.94	0.13
HD 210702 b	5.93	14.7	63.1	2	1.99	97.25	6.61	1.54	1.88
HD 81688 b	5.41	13.5	49.8	2.7	2.19	91.05	6.76	1.83	7.47
HD 87883 b	7.57	23.2	141.2	12.1	1.13	159.09	6.86	1.13	0.1
HD 5319 b	8.05	27.8	182.1	1.94	2.35	191.36	6.88	1.05	0.87
HD 158038 b	7.64	23.9	146	1.8	2.31	164.4	6.89	1.13	1.47
HD 117207 b	7.26	20.9	119.9	2.06	1.4	144.8	6.92	1.21	0.14
HD 154857 b	7.25	20.8	118.8	1.8	1.54	145.09	6.98	1.22	0.94

ups And c	4.09	11.9	28.5	14.57	1.37	97.46	8.2	3.42	0.89
HD 69830 b	5.95	14.8	63.7	0.033	0.95	103.51	7.01	1.63	
HD 1461 b	6.64	17.3	88.2	0.0239	1.3	121.69	7.01	1.38	8.11
HD 145457 b	6.57	17	88.2	2.9	2.29	122.23	7.19	1.39	6.07
HIP 11952 c	9.78	58	542.9	0.78	1.85	418.55	7.22	0.77	10.74
HD 170469 b	8.21	29.6	199.1	0.67	1.83	216.09	7.3	1.09	0.26
HD 148427 b	6.89	18.6	99.7	0.96	1.84	136.06	7.31	1.36	1.62
Gl 179 b	11.96	164	3200.1	0.82	1.36	1214.25	7.4	0.38	0.08
HD 136418 b	7.88	26.1	165.9	2	2.02	193.98	7.44	1.17	1.2
HD 28254 b	7.71	24.5	151.5	1.16	1.57	184.18	7.53	1.22	0.32
HD 231701 b	8.97	40.6	313.3	1.08	2.21	315.95	7.78	1.01	1.2
HD 173416 b	6.06	15.1	70.6	2.7	2.39	120.15	7.96	1.7	5.42
HAT-P-17 c	10.54	82.2	965.2	1.4	2.41	665.75	8.1	0.69	0.15
HIP 75458 b	3.31	11.5	21.4	8.82	1.47	93.29	8.1	4.36	4.67
HD 171028 b	8.31	30.8	211	1.98	1.71	250.34	8.13	1.19	0.69
HD 30856 b	8.07	28	184.2	1.8	2.26	234.74	8.37	1.27	0.98
HD 177830 b	7.18	20.4	115.2	1.49	2.11	173.36	8.51	1.51	1.15
HD 4203 b	8.68	35.9	262.3	2.07	2.16	308.14	8.59	1.17	0.54
HD 167042 b	5.97	14.8	64.3	1.6	2.02	127.31	8.59	1.98	1.54
HD 73526 b	9	41.1	320	2.9	2.22	353.99	8.61	1.11	1.06
HD 33564 b	5.08	12.9	43	9.1	1.45	113.39	8.79	2.63	0.47
HD 82943 b	6.54	16.9	84.1	1.75	1.57	149.8	8.87	1.78	0.44
HD 86264 b	7.42	22.1	130.2	7	2.18	198.3	8.98	1.52	0.31
HD 75898 b	8.04	27.7	181.1	2.51	2.21	251.66	9.08	1.39	0.63
HD 142 b	5.7	14.1	56.8	1.03	1.36	128.38	9.11	2.26	0.41
HIP 57274 c	8.96	40.4	311.5	0.41	1.53	370.27	9.17	1.19	1.81
HD 76700 b	8.13	28.7	190.4	0.197	1.77	264.53	9.22	1.39	12.77
HIP 57050 b	11.9	159	3022.6	0.298	1.42	1467.52	9.23	0.49	1.17
6 Lyn b	5.86	14.5	61.1	2.4	2.15	134.24	9.26	2.2	1.1
HD 1690 b	9.17	44.2	357.1	6.1	2.41	412.43	9.32	1.15	5.98
HD 73534 b	8.24	30	202.6	1.15	2.36	282.47	9.42	1.39	0.39
24 Sex b	7.38	21.8	127.5	1.99	2.41	206.69	9.49	1.62	1.72
Gl 581 c	10.55	82.9	969.3	0.017	0.96	802.04	9.67	0.83	1.97
HD 98219 b	8.21	29.6	199.1	1.8	2.4	287.69	9.72	1.44	1.71
HD 208487 b	7.48	22.5	134.5	0.413	2.1	219.31	9.75	1.63	1.07
HD 126614 b	8.81	38	284.7	0.38	2.41	373.27	9.82	1.31	0.22
HD 89744 b	5.74	14.2	57.8	7.2	1.8	139.62	9.84	2.41	1.14
HD 2039 b	9.01	41.3	322	4.9	2.15	406.51	9.85	1.26	0.26
HD 183263 c	7.86	25.9	164	3.82	2.04	255.96	9.88	1.56	0.13
HD 205739 b	8.56	31	244.5	1.37	2.34	308.29	9.94	1.26	0.7
HD 109246 b	8.77	37.3	277.1	0.77	2.12	372.1	9.98	1.34	1.46
HD 177830 c	7.18	20.4	115.2	0.15	2.29	204.47	10.04	1.78	2.73
HD 62509 b	1.15	11.2	13	2.9	2.15	112.85	10.08	8.69	2.43

HD 162020 b	9.18	44.4	359.4	14.4	1.74	450.27	10.13	1.25	4.56
HD 73526 c	9	41.1	320	2.5	2.41	417.41	10.15	1.3	0.67
HD 43197 b	8.95	40.2	310	0.6	2.13	414.19	10.29	1.34	0.52
HD 125612 d	8.31	30.8	211	7.2	2.14	318.15	10.33	1.51	0.12
HD 20868 b	9.92	61.8	601	1.99	2.15	639	10.34	1.06	0.4
HD 192699 b	6.44	16.5	80.2	2.5	2.4	171.35	10.4	2.14	1.71
HD 30562 b	5.77	14.3	62.2	1.29	1.62	148.74	10.44	2.39	0.33
HD 68988 b	8.21	29.6	199.1	1.9	2.32	314.77	10.63	1.58	7.6
HD 52265 b	6.3	15.9	75	1.05	1.71	169.79	10.66	2.26	1.18
HD 122430 b	5.48	13.6	51.4	3.71	1.83	146.31	10.76	2.85	10.45
γ 1 Leo b	2.01	11.3	14.9	8.78	1.48	121.41	10.78	8.13	12.46
HD 156668 b	8.42	32.2	224.7	0.0131	1.57	349.3	10.84	1.55	6.83
HIP 13044 b	9.94	62.4	609.9	1.25	2.29	691.27	11.09	1.13	26.94
kappa CrB b	4.79	12.5	38	1.8	2.32	139.9	11.19	3.68	0.81
HD 168443 b	6.92	18.8	101.2	7.659	1.58	211.3	11.25	2.09	2.42
HD 219828 b	8.04	27.7	181.1	0.066	2.4	314.01	11.33	1.73	15.4
HD 16175 b	7.28	21	121	4.4	2.28	240.53	11.45	1.99	0.42
HIP 14810 b	8.52	33.6	238.3	3.88	2.12	387.28	11.53	1.63	6.85
HD 202206 b	8.08	28.1	185.2	17.4	2.22	326.05	11.6	1.76	0.58
61 Vir b	4.74	12.4	37.2	0.016	1.25	145.35	11.68	3.91	8.81
HD 125612 b	8.31	30.8	211	3	2.3	366.11	11.89	1.74	0.36
HD 222582 b	7.7	24.4	150.6	7.75	1.85	294.2	12.06	1.95	0.4
HD 28185 b	7.81	25.4	159.8	5.7	2.38	308.53	12.15	1.93	0.47
HD 11506 c	7.51	22.8	136.4	0.82	2.17	278.42	12.23	2.04	1.02
HIP 11952 b	9.78	58	542.9	2.93	2.41	710.6	12.25	1.31	0.93
HD 74156 b	7.62	23.7	145	1.88	2.31	291.84	12.31	2.01	2.63
HD 74156 c	7.62	23.7	145	8.03	2.31	291.84	12.31	2.01	0.23
HD 96127 b	7.43	22.1	130.8	4	1.64	273.46	12.35	2.09	11.63
HD 88133 b	8.01	27.4	178.2	0.22	2.41	339.9	12.41	1.91	19.31
HD 183263 b	7.86	25.9	164	3.67	2.29	323.19	12.48	1.97	0.38
mu Ara c	5.15	13	44.4	0.03321	1.5	162.76	12.52	3.67	6.44
HD 202206 c	8.08	28.1	185.2	2.44	2.31	351.87	12.52	1.9	0.19
HD 108874 c	8.76	37.1	275.4	1.018	2.36	469.48	12.65	1.7	0.22
HD 188015 b	8.22	29.7	200.3	1.26	2.31	376.73	12.68	1.88	0.44
HD 164509 b	8.24	30	202.6	0.48	2.41	382.02	12.75	1.89	0.57
HD178911Bb	7.98	27.1	175.3	6.292	2.19	350.71	12.94	2	1.69
HD 179079 b	7.95	26.8	172.4	0.08	2.21	348.77	13.01	2.02	6.34
GJ 3634 b	11.95	163.1	3157.9	0.022	2.26	2125.97	13.03	0.67	7.3
HD 104985 b	5.79	14.3	59.2	6.3	2.39	187.25	13.08	3.17	6.49
HD 108874 b	8.76	37.1	275.4	1.36	2.41	488.4	13.16	1.77	0.55
HD 12661 c	7.44	22.2	131.2	1.57	1.99	292.32	13.17	2.23	0.21
HD 142415 b	7.34	21.5	124.9	1.62	2.01	287.21	13.37	2.3	0.46

HD 148156 b	7.69	24.3	149.8	0.85	2.41	327.39	13.47	2.19	0.23
HD 11964 b	6.42	16.4	79.4	0.622	1.82	220.87	13.48	2.78	0.32
HD 145377 b	8.12	28.6	189.4	5.76	2.4	386.81	13.53	2.04	1.2
HD 168746 b	7.95	26.8	172.4	0.23	1.83	362.82	13.54	2.1	8.13
HD 200964 b	6.64	17.3	88.2	1.85	2.41	236.34	13.62	2.68	1.26
HD 169830 c	5.9	14.6	62.2	4.04	2.16	199.75	13.67	3.21	0.24
HD 38529 b	5.94	14.7	63.4	0.78	2.29	201.71	13.69	3.18	8.73
HD 23596 b	7.24	20.7	118	8.1	2.33	284.15	13.73	2.41	0.34
HD 9446 b	8.35	31.3	215.8	0.7	2.26	430.23	13.73	1.99	2.51
HD 96063 b	8.37	31.6	218.3	0.9	2.32	434.59	13.76	1.99	2.12
HD 6718 b	8.45	32.6	228.7	1.56	2.23	454.68	13.94	1.99	0.14
HD 163607 b	8.15	28.9	192.6	0.77	2.39	403.1	13.95	2.09	2.13
HD 216770 b	8.1	28.4	187.3	0.65	1.96	399.02	14.07	2.13	1.03
HD 99492 b	7.38	21.8	127.5	0.109	1.59	307.25	14.11	2.41	3.68
HIP 14810 d	8.52	33.6	238.3	0.57	2.35	475.85	14.17	2	0.25
HD 163607 c	8.15	28.9	192.6	2.29	2.41	411.88	14.25	2.14	0.32
HD 31253 b	7.13	20	112.3	0.5	2.28	287.83	14.36	2.56	0.64
HD 154672 b	8.22	29.7	200.3	5.02	2.39	427.73	14.4	2.14	1
HD 73267 b	8.9	39.4	301.2	3.06	2.32	571.49	14.5	1.9	0.22
HD 290327 b	8.96	40.4	311.5	2.54	2.38	587.28	14.54	1.89	0.14
HD 113538 b	9.02	41.5	324.1	0.27	1.88	604.32	14.58	1.86	0.44
HIP 14810 c	8.52	33.6	238.3	1.28	2.39	489.51	14.58	2.05	0.87
HD 187123 b	7.86	25.9	164	0.52	2.25	377.74	14.58	2.3	12.99
HD 169830 b	5.9	14.6	62.2	2.88	2.23	213.59	14.61	3.43	1.07
HD 73256 b	8.08	28.1	185.2	1.87	2.32	411.13	14.63	2.22	11.45
HD 213240 b	6.8	18.1	95.4	4.5	2.17	266.12	14.67	2.79	0.35
HD 217107 b	6.16	15.4	70.2	1.33	1.67	226.65	14.7	3.23	6.98
7 CMa b	3.96	11.8	27.1	2.6	2.2	176.24	14.94	6.51	0.57
HD 49674 b	8.1	28.4	187.3	0.115	2.41	425.06	14.99	2.27	7.71
HD 38529 c	5.94	14.7	63.4	17.7	2.41	223.49	15.17	3.53	0.31
HD 11506 b	7.51	22.8	136.4	3.44	2.41	346.03	15.19	2.54	0.27
HD 190984 b	8.76	37.1	275.4	3.1	2.38	575.12	15.5	2.09	0.13
HD 25171 b	7.79	25.2	157.8	0.95	2.35	390.77	15.51	2.48	0.18
HD 9446 c	8.35	31.3	215.8	1.82	2.41	487.44	15.56	2.26	0.73
HD 196050 b	7.5	22.7	135.9	2.83	2.4	355.03	15.64	2.61	0.25
HD 50554 b	6.86	18.4	97.8	5.16	1.93	288.93	15.7	2.95	0.22
HD 8535 b	7.7	24.4	150.6	0.68	2.41	383.88	15.73	2.55	0.23
HD 117618 b	7.18	20.4	115.2	0.178	2.05	321.65	15.79	2.79	3.19
HD 102117 b	7.47	22.5	133.6	0.172	2.12	355.28	15.82	2.66	3.91
HD 190360 b	5.71	14.1	57	1.502	1.7	225.13	15.95	3.95	0.14
HD196885Ab	6.4	16.3	78.6	2.98	2.34	260.42	15.97	3.31	0.32
HD 152581 b	8.54	33.9	241.2	1.5	2.36	546.33	16.14	2.27	1.51

HD 153950 b	7.39	21.8	128.2	2.73	2.29	352.69	16.14	2.75	0.49
30 Ari B b	7.1	19.9	110.6	9.88	2.22	323.35	16.28	2.92	0.54
HD 137388 b	8.71	36.3	266.5	0.223	2.28	591.92	16.31	2.22	0.44
HD 187123 c	7.86	25.9	164	1.99	2.38	422.69	16.32	2.58	0.11
tau Boo b	4.5	12.2	33.6	3.9	2.01	200.8	16.46	5.97	13.64
HD 156411 b	6.67	17.5	89.5	0.74	2.31	288.28	16.48	3.22	0.54
HD 39091 b	5.67	14	56	10.3	1.83	232.09	16.55	4.14	0.3
HD 45350 b	7.88	26.1	165.9	1.79	2.32	436.22	16.74	2.63	0.31
HD 30177 b	8.41	32.1	223.4	7.7	2.41	543.02	16.92	2.43	0.2
HD 82886 b	7.78	25.1	156.7	1.3	2.39	426.24	16.98	2.72	1.36
Gl 581 d	10.55	82.9	969.3	0.019	1.27	1409.26	17	1.45	0.66
HD 185269 b	6.67	17.5	89.5	0.94	2.41	298.27	17.05	3.33	11.48
HD 139357 b	5.98	14.8	64.6	9.76	2.35	254.74	17.16	3.94	2.26
HD 13931 b	7.61	23.6	143.5	1.88	2.25	407.94	17.29	2.84	0.11
HD 69830 c	5.95	14.8	63.7	0.038	1.5	255.89	17.34	4.02	2.27
HD 7449 c	7.5	22.7	135.9	2	2.29	400.76	17.65	2.95	0.1
HD 179949 b	6.25	15.7	73.3	0.95	2.34	280.73	17.84	3.83	12.52
alf Ari b	2.01	11.3	14.9	1.8	2.32	201.46	17.89	13.49	5.39
HD 141937 b	7.25	20.8	118.8	9.7	2.32	374.61	18.01	3.15	0.33
Gl 581 b	10.55	82.9	969.3	0.05	1.31	1493.45	18.02	1.54	3.54
HD 92788 b	7.31	21.3	123	3.86	2.41	383.5	18.04	3.12	0.49
HD 12661 b	7.44	22.2	131.2	2.3	2.35	406.9	18.33	3.1	0.64
HD 7449 b	7.5	22.7	135.9	1.11	2.34	416.66	18.35	3.07	0.21
HD 102195 b	8.05	27.8	182.1	0.45	2.29	513.42	18.46	2.82	8.12
HD 69830 d	5.95	14.8	63.7	0.058	1.55	273.71	18.55	4.3	0.67
HD 217786 b	7.8	25.3	158.9	13	2.41	470.58	18.61	2.96	0.25
HD 168443 c	6.92	18.8	101.2	17.193	2.04	352.44	18.76	3.48	0.25
HD 218566 b	8.63	35	239.3	0.21	2.38	658.54	18.82	2.75	0.6
HD 83443 b	8.23	29.9	201.5	0.4	2.33	564.02	18.89	2.8	12.15
HD 23079 b	7.1	19.9	110.6	2.5	2.32	375.54	18.91	3.39	0.36
HD 82943 c	6.54	16.9	84.1	2.01	2.33	327.55	19.39	3.9	0.71
Gliese 876 e	10.17	69.3	724.3	0.046	1.34	1354.65	19.56	1.87	0.52
HD 32518 b	6.44	16.5	80.2	3.04	2.22	323.35	19.63	4.03	8.07
HD 44219 b	7.69	24.3	149.8	0.58	2.39	480.61	19.78	3.21	0.52
HD 19994 b	5.07	12.9	42.9	1.68	2.34	256.15	19.89	5.98	0.64
γ Cephei b	3.22	11.5	20.8	1.85	2.31	229.82	20.02	11.06	1.12
HD 81040 b	7.72	24.6	152.3	6.86	2.33	493.51	20.1	3.24	0.21
HD 114729 b	6.69	17.6	90.1	0.84	1.91	354.54	20.14	3.93	0.33
HD 7199 b	8.06	27.9	183.1	0.29	2.3	562.17	20.15	3.07	0.34
HD 16141 b	6.78	18	93.9	0.215	2.1	362.79	20.15	3.86	1.35
55 Cnc f	5.95	14.8	63.7	0.144	1.71	299.58	20.3	4.7	0.57
HD142022Ab	7.7	24.4	150.6	5.1	2.41	496.53	20.35	3.3	0.11

BD+48738 b	9.14	43.7	350.2	0.91	2.41	890.79	20.4	2.54	5.12
HD 113538 c	9.02	41.5	324.1	0.71	2.24	858.31	20.7	2.65	0.13
51 Peg b	5.49	13.6	51.6	0.468	2.04	282.8	20.76	5.48	11.49
HD 72659 b	7.46	22.4	132.9	3.15	2.25	470.28	21.01	3.54	0.14
16 Cyg B b	6.2	15.6	71.6	1.68	1.99	327.63	21.06	4.58	0.28
HD 114762 b	7.3	21.2	122.4	10.98	1.94	448.97	21.18	3.67	1.66
HIP 57274 d	8.96	40.4	311.5	0.527	2.34	860.95	21.31	2.76	0.32
HD 89307 b	7.06	19.6	108.4	1.78	2.31	423.99	21.62	3.91	0.15
61 Vir c	4.74	12.4	37.2	0.0573	1.7	270.43	21.72	7.27	2.04
HD 20367 b	6.41	16.3	79	1.07	2.14	356.92	21.83	4.52	0.45
HD 46375 b	7.94	26.7	171.5	0.249	2.4	583.2	21.84	3.4	11.59
70 Vir b	5	12.8	41.6	6.6	1.68	281.04	22	6.76	1.92
HIP 57274 b	8.96	40.4	311.5	0.036	2.39	904.73	22.39	2.9	4.66
Gj 849 b	10.42	77.7	878.2	0.99	2.25	1773.6	22.81	2.02	0.11
HD 40979 b	6.74	17.6	93	3.28	2.41	405.07	23.02	4.36	0.69
HD 195019 b	6.91	18.8	101.1	3.7	2.41	435.61	23.17	4.31	4.7
HD 128311 c	7.51	22.8	136.4	3.21	2.11	529.68	23.26	3.88	0.2
HD 106252 b	7.36	21.6	126	7.56	2.35	502.61	23.27	3.99	0.19
HD 70642 b	7.17	20.3	114.6	2	2.37	472.62	23.27	4.12	0.12
HD 10697 b	6.29	15.9	74.7	6.38	2.41	370.2	23.31	4.96	0.37
HD 114386 b	8.73	36.6	270.4	1.24	2.39	855.84	23.36	3.17	0.22
HD 11964 c	6.42	16.4	79.4	0.079	2.41	384.9	23.49	4.85	4.47
HD 1461 c	6.64	17.3	88.2	0.0186	2.39	413.07	23.81	4.68	4.65
61 Vir d	4.74	12.4	37.2	0.072	1.79	298.13	23.95	8.02	0.93
HD 164922 b	7.01	19.3	105.8	0.36	2.23	472	24.44	4.46	0.2
HD 134987 b	6.45	16.5	80.5	1.59	2.35	405.98	24.59	5.04	0.73
HD 114783 b	7.57	23.2	141.2	1	2.41	577.47	24.89	4.09	0.31
HD 47536 b	5.25	13.2	46.4	5	1.86	330.69	25.12	7.13	6.78
ups And b	4.09	11.9	28.5	0.69	2.41	301.98	25.42	10.6	13.03
ups And e	4.09	11.9	28.5	1.059	2.41	302.21	25.44	10.61	0.15
HD 4208 b	7.79	25.2	157.8	0.8	2.41	644.9	25.59	4.09	0.24
HR 810 b	5.4	13.4	49.6	2.26	2.25	346.36	25.77	6.98	0.94
HD 134987 c	6.45	16.5	80.5	0.82	2.41	428	25.92	5.31	0.1
HD 216437 b	6.06	15.1	70.2	1.82	2.32	402.41	26.65	5.73	0.22
HD 128311 b	7.51	22.8	136.4	2.18	2.26	611.39	26.85	4.48	0.32
HD 37124 c	7.68	24.2	149.1	0.652	2.32	657.97	27.19	4.41	0.23
HD 27442 b	4.44	12.1	32.8	1.35	2.38	331.05	27.36	10.09	2.65
HD 75289 b	6.35	16.1	79.4	0.42	2.41	442.32	27.47	5.57	12.86
HD 3651 b	5.8	14.3	59.4	0.2	1.71	395.71	27.59	6.66	1.58
HD 130322 b	8.05	27.8	182.1	1.02	2.41	782.5	28.13	4.3	4.5
GJ 3021 b	6.59	17.1	86.1	3.37	2.15	481.99	28.16	5.6	0.87
42 Dra b	4.83	12.6	38.6	3.88	2.01	354.32	28.22	9.17	8.61
Gliese 876 c	10.17	69.3	724.3	0.7142	1.62	1983.05	28.63	2.74	1.34

55 Cnc c	5.95	14.8	63.7	0.169	2.04	427.1	28.94	6.71	1.86
HD 37124 b	7.68	24.2	149.1	0.675	2.4	704.49	29.11	4.73	0.73
HD 37124 d	7.68	24.2	149.1	0.696	2.41	706.1	29.18	4.74	0.14
HD 10647 b	5.52	13.7	56.8	0.93	2.41	404.82	29.55	7.13	0.26
HD 192263 b	7.79	25.2	157.8	0.72	2.41	746.56	29.63	4.73	2.39
HD 217107 c	6.16	15.4	70.2	2.49	2.38	459.07	29.77	6.54	0.1
mu Ara e	5.15	13	44.4	1.814	2.32	387.93	29.84	8.74	0.11
HD 99492 c	7.38	21.8	127.5	0.36	2.31	650.41	29.87	5.1	0.08
47 Uma b	5.1	12.9	43.4	2.53	2.21	387.57	29.99	8.92	0.28
mu Ara b	5.15	13	44.4	1.676	2.34	394.52	30.34	8.89	0.39
55 Cnc b	5.95	14.8	63.7	0.824	2.09	450.04	30.49	7.07	3.9
mu Ara d	5.15	13	44.4	0.5219	2.38	407.36	31.33	9.18	0.64
GJ 176 b	9.97	63.4	627.2	0.0265	2.39	2003.36	31.6	3.19	3.89
HD 6434 b	7.72	24.6	152.3	0.39	2.4	776.12	31.61	5.1	1.97
HD 190360 c	5.71	14.1	57	0.057	2.41	451.31	31.97	7.91	4.44
HD 7924 b	7.185	20.4	115.5	0.029	2.36	678.95	33.28	5.88	6.54
47 Uma d	5.1	12.9	43.4	1.64	2.34	435.6	33.71	10.03	0.05
14 Her b	6.67	17.5	89.5	4.64	2.41	604.59	34.56	6.75	0.12
47 Uma c	5.1	12.9	43.4	0.54	2.38	449.65	34.79	10.35	0.16
HD 4308 b	6.54	16.9	84.1	0.0405	2.34	635.09	37.59	7.55	3.71
55 Cnc d	5.95	14.8	63.7	3.835	2.41	598.33	40.54	9.4	0.08
Gl 86 b	6.17	15.5	70.6	4.01	2.22	646.04	41.8	9.16	3.7
HD 147513 b	5.37	13.4	48.9	1.21	2.4	570.14	42.6	11.65	0.36
Gl 785 b	6.13	15.3	69.2	0.053	2.19	659.98	43.08	9.53	1.02
HD 192310 c	5.73	14.2	57.6	0.075	2.36	733.4	51.77	12.74	0.28
eps Eridanib	3.73	11.7	24.8	1.55	2.36	677.76	58.04	27.29	0.13
Gl 581 e	10.55	82.9	969.3	0.0061	2.38	4936.46	59.55	5.09	5.34
Gliese 876 d	10.17	69.3	724.3	0.021	2.36	4213.6	60.84	5.82	8.53
Gliese 876 b	10.17	69.3	724.3	2.2756	2.41	4373.92	63.15	6.04	0.85